1-1-2010

Fractal fluctuations in the cardiovascular dynamical system : from the autonomic control to the central nervous system influence

Asif Hasa Sharif
Ryerson University

FRACTAL FLUCTUATIONS IN THE CARDIOVASCULAR DYNAMICAL SYSTEM: FROM THE AUTONOMIC CONTROL TO THE CENTRAL NERVOUS SYSTEM INFLUENCE

By

Asif Hasan Sharif

B. Sc. (Hons), University of Toronto, 2003

M. A. Sc., Ryerson University, 2006

A dissertation

presented to Ryerson University

in partial fulfillment of the

requirement for the degree of

Doctor of Philosophy

in the Program Of

Mechanical Engineering

Toronto, Ontario, Canada, 2010

Author's Declaration

I hereby declare that I am the sole author of this dissertation.

I authorize Ryerson University to lend this dissertation to other institutions or individuals for the purpose of scholarly research.

Signature _____

I further authorize Ryerson University to reproduce this dissertation by photocopying or by other means, in total or in part, at the request of other institutions or individuals for the purpose of scholarly research.

Signature _____

Abstract

Fractal Fluctuations in the Cardiovascular Dynamical System: From the Autonomic Control to the Central Nervous System Influence

Asif Sharif

Doctor of Philosophy

Department of Mechanical and Industrial Engineering, Ryerson University

2010

The fractal component in the complex fluctuations of the human heart rate represents a dynamic feature that is widely observed in diverse fields of natural and artificial systems. It is also of clinical significance as the diminishing of the fractal dynamics appears to correlate with heart disease processes and adverse cardiac events in old age. While the autonomic nervous system directly controls the pacemaker cells of the heart, it does not provide an immediate characterization of the complex heart rate variability (HRV). The central nervous system (CNS) is known to be an important modulator for various cardiac functions. However, its role in the fractal HRV is largely unclear.

In this research, human experiments were conducted to study the influence of the central nervous system on fractal dynamics of healthy human HRV. The head up tilt (HUT) maneuver is used to provide a perturbation to the autonomic nervous system. The subsequent fractal effect in the simultaneously recorded electroencephalography and beat-to-beat heart rate data was examined. Using the recently developed multifractal factorization technique, the common multifractality in the data fluctuation was analyzed. An empirical relationship was uncovered

which shows the increase (decrease) in HRV multifractality is associated with the increase (decrease) in multifractal correlation between scale-free HRV and the cortical expression of the brain dynamics in 8 out of 11 healthy subjects. This observation is further supported using surrogate analysis.

The present findings imply that there is an integrated central-autonomic component underlying the cortical expression of the HRV fractal dynamics. It is proposed that the central element should be incorporated in the fractal HRV analysis to gain a more comprehensive and better characterization of the scale-free HRV dynamics. This study provides the first contribution to the HRV multifractal dynamics analysis in HUT. The multivariate fractal analysis using factorization technique is also new and can be applied in the more general context in complex dynamics research.

Acknowledgement

I would like to express my deep gratitude to my supervisor Dr. Bill Lin for his continuous support, guidance and patience. I had many stimulating discussions with Dr. Lin that taught me valuable research skills and gave me the confidence to approach and solve complex problems. This work would not have been possible without him. I also thank Dr. Hon Kwan (Department of Physiology, University of Toronto), who was my undergraduate supervisor, and the first person to introduce me to the world of fractals. He has always been a source of guidance and inspiration.

I thank my parents, Mohammed and Rahena Tayab, for their unconditional love. They have supported me through very difficult circumstances of their own and encouraged me to follow my dreams and given me the confidence and opportunity to do so. I thank my brother, Adeeb Sharif who has shared my struggles, loses and successes throughout life.

I thank the staff and faculty of the Department of Mechanical Engineering at Ryerson University for their support and technical help.

I look forward to many great memories with my lovely fiancé Aisha Ghafoor. Among my friends, I thank Ahmed El Saadany and Jean-Jacques Boileau-Bekuit for all the adventures we had together. I also thank John Zamiska, Maher Azem, and Balaji Venkatesh.

To my mom,

  Rahena Tayab

and my dad,

  Mohammed Tayab

"O my Sustainer, Inspire me so that I may forever be grateful for those blessings of Thine with which Thou hast graced me and my parents, and that I may do what is right that will meet with Thy goodly acceptance; and grant me righteousness in my offspring. Verily, unto Thee have I turned in repentance: for, verily, I am of those who have surrendered themselves unto Thee"

  - (Al-Ahqaf, 15, Quran)

Table of Contents

List of Figures

List of Tables

List of Appendices

Nomenclature

$A_{LF/HF}$ sympatho-vagal index

$|T_\psi[x](t,a)|$ wavelet coefficient modulus maxima

a scale

b *theta*, *alpha* or *beta*

d LF, HF or LF/HF

$e(s)$ EEG without the electroocular artifacts

e_A aggregated EEG

$e_{Apr}(n)$ iAAFT aggregated EEG

$e_{As}(n)$ randomly permutated aggregated EEG

E_j EEG interval corresponding to the RRi segment

$f(\alpha_{\pi/\mu})$ Multifractal spectrum of π relative to μ

$f(\alpha)$ Hausdorff dimension of the support α

$f(\alpha_1, \alpha_2)$ Hausdorff dimension of the support of (α_1, α_2)

G UPR or SUP

$L(0)$ $\{(q, p), \tau(q, p) = 0\}$

P normalized spectral power

$P(f)$ Lomb periodogram

q moment

R relative EEG-ANS index

$r(n)$ interval between two R waves

$r_{pr}(n)$ iAAFT RRi

$r_s(n)$ randomly permutated RRi

T	change in R from SUP to UPR
$T_\psi[x](t,a)$	wavelet coefficient of $x(t)$
U_v	$W_v^{UPR}\left(I_q\right)/W_c^{SUP}\left(I_q\right)$
U_{RE}	$W_{R/E}^{UPR}\left(I_q\right)/W_{R/E}^{SUP}\left(I_q\right)$
v	EEG or RRi
$W(I_q)$	width of (relative) singularity spectrum at $q \in I_q = [q_{min}, q_{max}]$
$Z(a;q,p)$	joint partition function
α	Hölder Exponent
γ	uniform random variable
ρ_p	functional difference in the p-direction
ρ_q	functional difference in the q-direction
$\tau_{\pi/\mu}$	Common Multifractal Factor of $\pi(\mu)$ relative to $\mu(\pi)$
$\tau(q)$	scaling function of the partition function
$\tau(q,p)$	scaling function of the joint partition function
$\psi(t)$	analyzing wavelet

Abbreviations

ANS	autonomic nervous system
CNS	central nervous system
CMF	common multifractal factor
CVLM	caudal ventrolateral medulla
DVN	dorsal vagal motor nucleus
EEG	electroencephalograph

HF	high frequency
HRV	heart rate variability
HUT	head up tilt
IML	intermediolateral cell column
JWTMM	joint wavelet transform modulus maxima
LF	low frequency
NA	nucleus ambiguus
NTS	nucleus of the solitary tract
PAG	midbrain pariaqueductal gray
PNS	parasympathetic nervous system
PVN	paraventricular nucleus of the hypothalamus
RRi	interval between two R waves
RVLM	rostral ventrolateral medulla
SNS	sympathetic nervous system
SUP	supine
UPR	upright at 75˚ after HUT maneuver

Chapter 1 Introduction

The beat-to-beat heart rate fluctuation of the human heart rate variability (HRV) has a fundamental scale-free dynamic component that is similarly observed in other natural systems. Examples are abundant, ranging from hydrodynamic turbulence [1], seismic wave activity [2], to social networking [3, 4], DNA sequences [5], the structure of the universe [6], gait interval [7], and market dynamics [8], just to name a few. The scale-free component of HRV cannot be immediately related to such external factors as physical activity [9, 10] and is believed to reflect the intrinsic property of human physiology. This "endogenous" effect also bears important health implications because there is a correlation between the diminishing multifractality of HRV and the deterioration of health in certain heart disease conditions [11-13], and with old age [14-16]. The study of the scale-free dynamics in human HRV is therefore not only of fundamental significance, but it also has a practical importance for the better understanding of cardiovascular health.

The fundamental cause for the abundance of scale-free dynamics in nature remains largely unclear. It may be that there is no general cause, but perhaps a case by case understanding of scale free dynamics. For example, it was shown that when the number of new trees introduced in a forest, exceed the number of trees set ablaze, the system enters a "critical state" [17]. In this state, the size and duration of forest fires have been shown to exhibit scale free fluctuation.

It is possible to gain detailed characterization of the scale-free fluctuations using the *fractal* model. A fractal has a distinct appearance which implies a "self-duplicative process" into ever finer scales ad infinitum. Most fractals found in natural and large artificial systems exhibit the highly "heterogeneous," *multifractal* scale-free structure with interwoven fractal subsets of

different characteristics [18, 19]. The scale-free component of human HRV is known to exhibit the multifractal property [11-13].

Although the scale-free property of HRV has been a subject of intense study, its dynamic origin and potential functional purpose remain unclear. While it is tempting to find clues from the vascular and respiratory functions, past studies actually concluded otherwise [20, 21]. Fortrat et al. [22] observed that changes in blood pressure variability (BPV) do not necessarily translate into HRV. In a prolonged, 42 day bed rest study, they showed that the dynamic pattern of BPV is distinctly different than that of HRV. Respiratory response, due to the cardiac-respiratory coupling known as the respiratory sinus arrhythmia mechanism, is a narrow band process in the high frequency range [23] and cannot explain the massive $1/f$-like signal power from the beat-to-beat heart rate data [24].

One potential source for multifractal HRV that is of significant importance is the central nervous system (CNS). The central influence in cardiac functions is well established [25]. Not only does the CNS respond to demands from the cardiovascular system, it can also triggers efferent responses to affect the autonomic control of heart rate in such events as the anticipation of threat [23] and the onset of exercise [26]. Whether there is a direct central influence on the HRV multifractal property is largely unclear. The literature on sleep [27] and mental exercise [28-30] suggests that such a link should exist. These past results are however based only on one (among infinite) scaling exponents of HRV. Furthermore, the specific CNS activity was not described in the studies.

The objective of this research is to examine the potential brain-heart interaction in scale-free HRV dynamics. It is hypothesized that there is a direct, measurable, central expression associated with multifractal HRV. It is assumed that a perturbation to the autonomic control of

the heart rate changes the brain-heart interaction that can be characterized by comparing the fractal properties of heart rate and brain activity data. In the analysis, the technical difficulty of comparing fractal properties must be addressed since different fractal generating mechanisms could have indistinguishable fractal appearance (and thus scaling exponents) due to finite resolution in the signal analysis [31]. In this research, the previously developed joint wavelet transform modulus maxima is extended to allow for estimating the fractal correlation between the heart rate and brain activity data. This novel technique considers the multifractal spectrum with infinite scaling exponents, which differentiates this study from the current literature.

To test the hypothesis, human experiments were conducted. The central idea of the experimental design is the introduction of an orthostatic challenge to perturb the autonomic control of the heart rate using the head up tilt (HUT) maneuver. Both heart rate and brain activity data were collected as the independent variables for the experiments and their fractal correlation determined. It is shown that such a central link can indeed be identified and characterized. In addition, the well-established frequency domain measures are used to provide a preliminary reference to the physiological basis underlying the central correlate of multifractal HRV.

To the best of the author's knowledge, these new contributions have not been reported before. Based on the central-autonomic fractal element in HRV, this work provides a new research paradigm that allows for a more complete analysis of the complex fluctuation in the cardiovascular dynamical system. In what follows, the pertinent literature review on the functional and anatomical evidence of the central-autonomic interaction is first presented. The organization of the results is given in six chapters and is summarized in the last section.

1.1 Literature Review

Neural control of the heart rate is mediated by the sympathetic (SNS) and the parasympathetic (PNS) branch of the autonomic nervous system (ANS) [11, 32, 33]. Under most physiological conditions, the activation of one branch is accompanied by the inhibition of the other [33]. The balance oscillates from the state of quiescence, when homeostatic negative feedback reflexes dominate via the PNS, to the state of excitation where the SNS activity predominates. The state of excitation is a response to either physical or psychological stress, when central excitatory mechanisms reinforced by peripheral positive feedback reflex enhance cardiovascular activity [34, 35].

The effect from the specific ANS branch to the scale-free HRV has been studied using pharmaceutical methods. In particular, the administration of a chemical compound that blocks adrenaline (such as metoprolol), the main neurotransmission agent for the SNS, is known to have a minor influence on the HRV multifractality [10]. However, the administration of the compound atropine, which suppresses PNS activity, resulted in a marked loss of multifractality [10, 36].

The PNS of the ANS therefore plays a critical role in "maintaining" the scale-free HRV dynamics. The critical structure of this effect appears to be related to the frontal cortex. In animal studies, Horst et al. [37] identified command centres of PNS activity in the rodent CNS. Verberne et al. [38] further showed that the presence of an important structure of the central ANS network in the prefrontal cortex of rats particularly in the suppression of the [38][37]SNS activity. Pharmacological suppression in the frontal cortex activity in humans, resulted in a reduction of both heart rate and HRV [39]. Neuroimaging studies have provided evidence that the prefrontal cortex may have a direct link to PNS activity [40-42]. Taken together, these

4

pharmacological and neuroimaging studies lend support to the role of the prefrontal cortex in mediating PNS activity.

The possible neural pathways that connect the prefrontal cortex to the heart may reside within the central ANS network as shown in Figure 1-1. The prefrontal, cingulate and insula cortex form an interconnected network with the amygdala, where information flows in both directions. The amygdala is thought to be a major point of integration from the higher brain centres to physiological responses, and can directly activate the SNS via the rostral ventrolateral medulla (RVLM) [43]. These connections have not been shown in the simplified Figure 1-1. It is thought to have projections to the paraventricular nucleus of the hypothalamus (PVN), and the pons, specifically the midbrain pariaqueductal gray (PAG) and parabrachial–pontine nuclei [44]. In the context of the neural pathway affecting the prefrontal cortex, it is thought to have excitatory effects on the neurons of the RVLM [25, 45]. The RVLM is under tonic inhibition by the caudal ventrolateral medulla (CVLM). Electrical stimulation of RVLM is associated with an increase in sympathetic activity [46]. SNS activity is mediated from the RVLM via preganglionic sympathetic efferents with cell bodies in the intermediolateral (IML) cell column. These efferents synapse with postganglionic sympathetic efferents that innervate the heart with the input from the CNS [23].

The hypothalamus PVN, PAG, and the pons have been associated with inhibitory effects on the nucleus of the solitary tract (NTS) [23]. The NTS also has ascending input to these areas of the brain, particularly relevant in the arterial baroreceptor reflex. The main innervation of the NTS comes from baroreceptors in the body [47]. It is involved in the inhibition of the RVLM via the CVLM [46]. PNS activity is mediated from the NTS to the dorsal vagal motor nucleus (DVN) and nucleus ambiguus (NA) to the heart via the preganglionic vagal efferents.
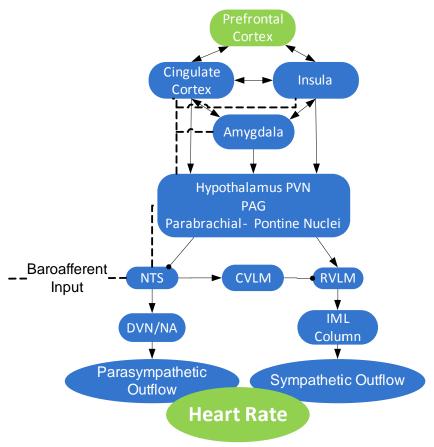
Figure 1-1 Pathway by which the prefrontal cortex might influence heart rate. " ⟷ "
bidirectional communication, " ⟶ " excitatory influence, "⟶•" inhibitory influence, and "
⁃⁃⁃⁃" baroafferent input.

The linkage between the CNS and HRV can also be seen in diseases that affect the brain.
There is an increased sympathetic control of HRV in certain epileptic patients [48]. Acute
cardiac events have further been hypothesized to explain the sudden unexplained death in
epileptic patients [49, 50]. Reduced HRV has also been associated with cerebrovascular risk
factors [51], Alzheimer's disease [52] and stroke patients with lesions [53].

The interaction between the CNS and HRV has been suggested by sleep studies based on
surface scalp potential data taken by electroencephalography (EEG) [54]. In sleep studies,
Brandenberger et al. have demonstrated an inverse coupling between delta wave activity in the

EEG and HRV [27]. Multifractality present in HRV from adults in wakefulness was present during rapid eye movement (REM) sleep but not in non-REM sleep [30]. Further evidence can be found in the changes of HRV properties reported with stress [55] and mental exercise [27-30].

In an animal study, Troncoso et al. [56] performed experiments to simultaneously analyze the EEG and HRV in response to light onset in awake rats. They found that light onset can induce a significant arousal in the brain with simultaneous enhancement of SNS activity in the HRV.

Naturally, the question that arises, is "how much of the multifractal HRV is correlated to EEG in humans?" The current understanding of HRV and EEG correlation is limited to the frequency domain and has not addressed multifractal HRV. While the joint study of multifractal objects has been explored before [31, 57, 58], only recently has an effective estimation of joint multifractality been possible. In particular, a common multifractal factor (CMF) shared by all the fractal sources can be calculated based on a novel technique known as the multifractal factorization [59]. In this research, the multifractal factorization approach is extended to define and characterize a CMF in the heart rate and EEG fluctuations.

1.2 Summary of Dissertation

This dissertation is divided into 6 chapters. Chapter 2 details the experimental method, data collection and processing. The experimental data will be analyzed using spectral methods in the frequency domain and singularity methods in the time domain. Their underlying ideas, working principle and numerical implementations are described in Chapter 3. The time domain approach and results, as well as its association with the spectral components, represent the main contribution of this research. In particular, the previously developed numerical technique of joint wavelet transform modulus maxima (JWTMM) [60] provides the basis to formulate the novel

multifractal factorization approach. Extensive numerical experiments based on random cascades are conducted to verify the fractal correlation analysis.

The application of these methods to the experimental data is arranged in the following two chapters. In Chapter 4, the results from the frequency domain analysis are shown. In Chapter 5, the results of the multifractal correlation analysis between the experimental heart rate and brain wave data are shown. To test for statistical significance, surrogate analyses were also performed to show that the captured multifractal correlation is not accidental. Chapter 6 discusses the results, and highlights the implications and limitations. Finally, the conclusions of the dissertation are summarized and possible future areas of research are identified.

Chapter 2   Experimental Investigation of Central and Autonomic Integration

2.1   *Background*

In this chapter, the experimental study of the CNS and ANS interaction is described. Separate tests were conducted on the subjects in supine (SUP) position and the upright (UPR) position after the HUT maneuver. The immediate physiological response due to HUT is mediated by the arterial baroreceptor reflex. Specifically, when in UPR, blood is pooled in the lower extremities due to the gravitational force. This causes a reduction in the venous return to the heart and, in turn, lowers the wall pressure of the carotid sinus and aortic arch. These effects are picked up by baroreceptors in the walls and the response is first relayed to the NTS which inhibits the CVLM, and leads to a reduction in the inhibition of the RVLM [20, 61, 62]. For large angle HUT, this chain of events triggers the physiological effect of increasing SNS efferent outflow and reducing PNS activity leading to a faster heart rate [63]. Hence, these effects can provide a known perturbation to the ANS and allows the systematic examination of a potential central component in fractal HRV.

The linkage between cardiovascular system and CNS has broader implications with respect to HUT. Ishibashi et al. [64] reported an increase in the heart rate at lower tilt angles after HUT, when auditory reaction time tasks were used, implicating the CNS influence in heart rate regulation. The effect of the ANS on brain activity has been explored in syncope studies. Ammirati et al. [65] conducted simultaneous EEG and heart rate recordings in HUT and reported a shift of the EEG signal power to a lower frequency range during the onset of syncope event in patients diagnosed with impaired vasovagal function. Using a 20 electrode montage and placing the electrodes strategically, Mercader et al. [66] suggested that the source of this phenomenon

originates in the left temporal lobe area. At the developmental stage, Grieve et al. [67] showed in a HUT study with infants between 0 to 4 months of age, that there was an increase in EEG power in the 12-50Hz window in the left frontal, right frontal, and occipital regions.

Given the extensive integration of the ANS in the higher brain centers [55], a HRV model including the central nervous system (CNS) provides a natural and appealing framework for further investigations. The strategy uses HUT to elicit a specific change in the ANS and simultaneously measure heart rate and EEG to analyze the cross "correlation" of their fluctuations.

2.2 Experimental Method & Materials

2.2.1 Subjects

In the literature, the sample sizes of exploratory HUT and HRV studies range from six to thirty five subjects [21, 27, 64, 68-70]. In this work, thirteen young adult subjects (9 males and 4 females. Age: 25.8 ±4.0 years old. Weight 69.5 ±11.2 kg. Height 172.4 ±8.4 cm) were recruited from the general university student population. Subjects with a history of mental health, cardiovascular, pulmonary or neurological conditions were excluded from the recruit. Subjects on medication and with a history of syncope were also excluded. The screening process relied mainly on the candidate's response to the questionnaire in the interview and was accepted in good faith.[1] The objectives, procedures, associated risks and risk management were described to each subject who then signed a consent form approved by the Ethics Board of Ryerson University [Appendix A]. Most subjects were dressed in casual wear during the experiment. There was no monetary compensation for their participation.

---

[1] It was found that 2 of the subjects had additional medical conditions that were not disclosed at the time of the experiment. Their data will be specified in the results.

10

2.2.2 Protocol

The experiment consisted of two parts conducted on two separate days at approximately the same time of the day (1~4 PM). The subjects were asked to maintain their normal daily activities, refrain from increased physical exercise, stimulants and have sufficient sleep two days prior to the recording sessions. The tests were conducted in a temperature controlled (22° C) shielded room under slightly dim lighting conditions (< 200 lx). During the test, subjects were asked to keep their eyes open, stay calm and relaxed.

The first part of the experiment consisted of the "baseline" recording. The subjects were asked to remain in the SUP position on the tilt table. The second part of the experiment is the HUT maneuver. Subjects were first put on the tilt table in the SUP position and allowed to settle down for ~10 mins before the HUT maneuver. They were then tilted to 75° UPR position. A registered nurse was present for this part of the experiment due to the potential for a syncope event. No case of syncope was recorded. The length of the SUP and UPR tests varied depending on the subjects, but they typically lasted for 40~50 mins.

2.3   Data Measurement

2.3.1 Background

To characterize the potential central influence in HRV, the brain and heart rate dynamics were recorded simultaneously. In this section, the background of these measurements and the specifics used in the experiments will be described.

The neural activity in the brain is physically carried out by the movement of ions in and out of the neuronal membrane. The movements produce electrical impulses known as the synaptic potential, which provides the means of communication between the neurons. Large numbers of neurons generating and conducting electrical impulses are detectable from the scalp

via the EEG recording. The recording involves placing electrodes on designated sites on the scalp. On average, the signal captured corresponds to cortical neuronal activity containing 10^7 to 10^9 neurons directly beneath the electrode [54, 71, 72][71, 72].

In this work, the bipolar measurement was used where the potential difference between adjacent electrodes are used to characterize the neuronal activities [72]. For this study, the electrodes were placed according to the International 10-20 system [73] at the frontal (FP1-FC3, FP2-FC4) sites. The gap between the electrode and the scalp was filled with low-impedance gel to facilitate conductivity (SIGNA Electrode Cream, Parker).

The beating of the heart is a result of the de/re-polarization process of the heart muscle cells. After the electric stimulation arrives at the sinoatrial node, the pacemaker cells of the heart, a chain reaction is triggered that leads to the massive, synchronized, movement of ions (mainly Na+, K+) in and out of the membrane of the heart muscle cells. While producing the muscle contraction of the myocardium, the massive ionic movement also results in measurable polarity difference that can be picked up by electrodes attached to the proper locations of the chest. [74].

2.3.2 Instrumentation

The recording device used in the experiment is a 16-bit ADC ambulatory recorder with a preset sampling rate at 256 Hz and, a hard-coded, band-passed filter (g.MobiLab, GTEC Inc, Austria); see Figure 2-1(a) . The filter in the recorder effects a [0.01, 100] Hz pass-band to the raw ECG signal and a [0.01, 30] Hz pass-band to the raw EEG signal. Note that the sampling rate of the recorder allows a Nyquist frequency at 128Hz, which is sufficient to cover the bandwidth of ECG and EEG activities. The output from the electrode is connected to a Personal Desktop Assistant (PDA). Impedance was measured using an electrode impedance meter (Mod EZM4A, Grass Instrument Co. MA, USA) that sent a test current less than 1μA at 30Hz. The

impedance was measured and found to be 20 ± 8.5 kΩ. In modern instruments with high input-impedance amplifiers, theoretical and experimental tests on EEG signal attenuation suggest that scalp impedances of upto 40 kΩ does not result in any significant amplitude attenuation [75].

The HUT maneuver was performed using a medical tilt table with foot rest, (Bailey Manufacturing Company, OH, USA); see Figure 2-1(b). It is capable of tilting from the supine (0º) position to the complete upright (90º) position.

(a)   (b)
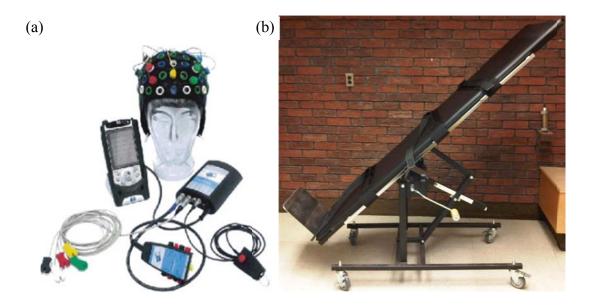
Figure 2-1 (a) g.Mobilab System (b) Tilt Table

2.3.3 Data Post-processing

The collected raw data need to be post-processed into proper forms for subsequent analyses. In this section, the postprocessing steps are explained and some sample data are shown.

A typical ECG record is depicted in Figure 2-2. The vertical lines mark the locations of the R wave. The R wave signifies the massive ionic movement mentioned above and corresponds to the pumping of the oxygen-rich blood from the left ventricle to the rest of the

body. The RR interval (RRi) taken as the interval between two R waves, $r(n)$, is used in the HRV analysis. Two channels of ECG were recorded from the two sets of electrodes attached to the chest and the RRi was extracted by cross-examining both sets to provide a greater level of assurance where $r(n)$ is. All records were visually checked for artifacts after the cross-examination. On average, 3779 uninterrupted RRi in SUP (mean ± SD: 0.964s ± 0.16s) and 5293 RRi in UPR (mean ± SD: 0.673s ± 0.12s) were collected.
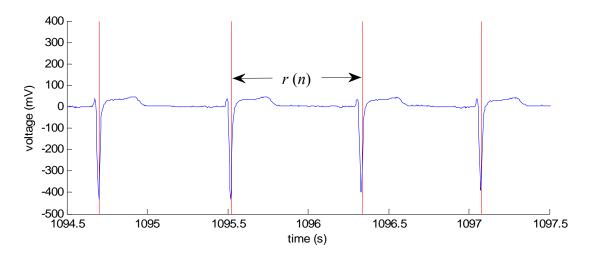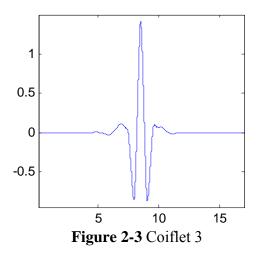
Figure 2-2 ECG record.

For the EEG, the 60 Hz AC is first filtered by a standard notch filter. Although the EEG captures electrical activity from the neurons in the CNS, it is often contaminated by artifacts of non-cerebral origin such as eye blinking, chin movement, and so on [76]. The most common type found in the long EEG recording is known as the electroocular artifact that is derived from eye blinking. There is extensive literature on effective ways to remove the electroocular artifacts [77, 78]. In this work, the method of wavelet filter using stationary wavelet transform and adaptive thresholding was adopted. First, the stationary wavelet transform is applied to the contaminated signal. The time-scale adaptive system is based on Stein's unbiased risk estimate (SURE). The optimal threshold is calculated by adaptively fine tuning the initial threshold value using a

14

gradient based adaptive algorithm. Finally, the inverse wavelet transform is applied to the thresholded wavelet coefficients to obtain EEG without the electroocular artifacts, $e(s)$. The algorithm, as well as its effectiveness, has been well documented in the references [79, 80].

To apply the stationary wavelet adaptive thresholding method, the mother wavelet chosen is the Coiflet 3 (Figure 2-3), as it resembles the EEG characteristics of an eye blink. The decomposition was done in six levels according to the dyadic scales. The thresholding was applied to the wavelet coefficients of the lowest 2 levels. They correspond to a frequency range of 0 to 2.3 Hz.

Figure 2-3 Coiflet 3

An example of a raw EEG segment contaminated with the large amplitude electroocular artifact (red curve) is shown in Figure 2-4(a). It is subsequently removed (blue curve) using the adaptive thresholding method. The approach is seen to work effectively and is able to retain the finer scale fluctuation in the raw EEG.

In Figure 2-4(b) the segments of the RRi from SUP and UPR are shown. Notice the diminishing large amplitude fluctuation going from SUP to UPR due to the withdrawal of the PNS activity. The lower mean RRi in SUP is also indicative of the SNS activation leading to a faster heart rate. The analysis and result reported in this work are based on the RRi and artifact removed EEG described above.
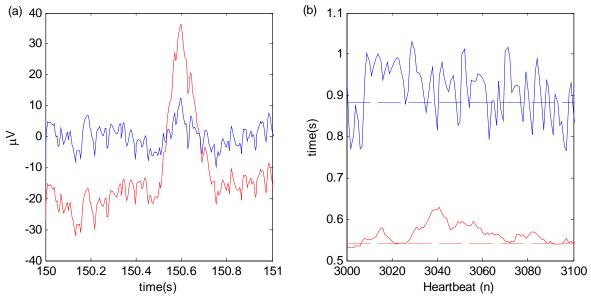
Figure 2-4 (a) EEG from S6. The recorded EEG is in red, which show a significant peak of duration less than 1 sec, characteristic of saccadic eye movement. The result after removing the artifact is in blue. (b) RRi from S6 in SUP (blue) and UPR (red). The mean RRi are shown as dashed lines.

Chapter 3   Data Analysis

In this chapter, the methods of analyses of the RRi and EEG are described. Both the spectral method in the frequency-domain and the fractal method in the time-domain are adopted. The frequency-domain approach is important for their better-known physiological correlates and, thus, provide a better understanding of our data in physiological terms. However, the spectral analysis does not describe the full detail of the RRi and EEG fractal fluctuation, nor is it able to capture the potential fractal correlation in their fluctuation. For these latter objectives, a novel technique was developed to extract fractal correlation in a jointly fluctuating time series. To the best of the author's knowledge, this technique is by far the only multivariate fractal tool that is able to characterize the fractal correlation of the fluctuation of multiple time series. The numerical example of coupled cascades is given to demonstrate this idea.

3.1   Frequency-Domain Methods

The power spectrum of the RR interval, $r(n)$ has been found to carry relevant physiological information in four major frequency bands: ultra low frequency (ULF), very low frequency (VLF), low frequency (LF), and high frequency (HF). The specific ranges of these bands are listed in Table 1 [11]; see also [81].

Table 1 Spectral Components of HRV

Variable	Frequency Range
ULF	≤ 0.003 Hz
VLF	$0.003 - 0.04$ Hz
LF	$0.04 - 0.15$ Hz
HF	$0.15 - 0.4$ Hz

The LF and HF components are of immediate importance to the current research due to their connection to the SNS and PNS activity [11, 82]. The study of ULF and VLF components remain difficult and inconclusive. In general, there is an intrinsic limit in analyzing very long time scale behavior in heart rate data, wherein different factors, such as the circadian rhythm, sleep cycles, can significantly shift the underlying dynamic regimes. The present study is further constrained to the limited time that a tilt test can be carried out. For these reasons, the dynamics in the ULF and VLF frequency bands are not studied in this research.

It should be noted that $r(n)$ does not have a natural time axis. If the time stamp is designated for each beat, one is faced with an unevenly spaced time series. For this reason, the frequency contents of $r(n)$ cannot be directly obtained by applying the Fourier transform. This issue can be resolved by using the so-called Lomb periodogram, which was developed to estimate the frequency contents from unevenly sampled time series [83]. In a nutshell, the Lomb periodogram adopts a "best fit" approach by minimizing the square difference between the projection of the signal onto the basis function of the transform and the original signal. This is known as the Lomb power spectral density method and is explained in Appendix B [83]. The Lomb periodogram of $r(n_i)$, $i = 1…N$, is defined as

$$P(f) = \frac{1}{2\sigma^2} \left\{ \frac{\left[\sum_{n=1}^{N} \left(r(t_n) - \bar{r} \right) \cos \left(2\pi f \left(t_n - \tau \right) \right) \right]^2}{\sum_{n=1}^{N} \cos^2 \left(2\pi f \left(t_n - \tau \right) \right)} + \frac{\left[\sum_{n=1}^{N} \left(r(t_n) - \bar{r} \right) \sin \left(2\pi f \left(t_n - \tau \right) \right) \right]^2}{\sum_{n=1}^{N} \sin^2 \left(2\pi f \left(t_n - \tau \right) \right)} \right\} \quad (3.1)$$

where $\bar{r}$ and σ^2 are the mean and variance of $r(t)$, f is the frequency and the value of τ is derived from

$$\tan\left(4\pi f\tau\right) = \frac{\sum_{n=1}^{N}\sin\left(4\pi f t_n\right)}{\sum_{n=1}^{N}\cos\left(4\pi f t_n\right)} \qquad (3.2)$$

Laguna et al. compared the Lomb method against the fast Fourier transform (FFT) and autoregressive estimate with linear and cubic interpolation on an integral pulse frequency modulation (IPFM) model. They showed that the Lomb method avoids the lowpass effect in the other methods when applied to unevenly sampled data [84]. Let RRi and its time stamp be $r(n)$, $t(n) = \sum_{l=1}^{n} r(l), n = 1,2,...,$ respectively. To track the subject's ANS activity, $r(n)$ is first segmented into intervals of K heart beats $Rj = \{r((j\text{-}1)K + 1), ..., r(jK)\}, j = 1, ..., N_K$. Results reported in the following chapters are based on intervals of $K = 128$-beat with 50% overlap (64-beat).

Similarly, EEG can be characterized via the correlation between specific spectral components and such physiological events as alertness, relaxation, and other cognitive functions. Of immediate importance to the current study is the *theta*, *alpha* and *beta* band property; see Table 2 [71]. These frequency bands reflect the general quality of attention (*theta*), focused relaxation (*alpha*) and alertness (*beta*) [85]. It is intuitive that these states can be altered by the HUT maneuver, and thus the frequency bands too. Indeed, Poupard et al. [86] showed that the alertness of healthy individuals is strongly correlated to the *beta* band power. In sleep deprived individuals, the postural change from SUP to UPR has the effect of enhancing alertness and the *beta* band power [87].

Table 2 Spectral Components of EEG.

Variable	Frequency Range
Delta	0 – 4 Hz
Theta	4 – 8 Hz
Alpha	8 – 13 Hz
Beta	13 – 30 Hz
Gamma	> 30 Hz

In the data analysis of the EEG, the same segmentation approach in the RRi data is used. In particular, the EEG interval corresponding to the RRi segment is first identified. For each R_j, the corresponding EEG interval $E_j = \{e(u_j\Delta t), \ldots, e(v_j\Delta t)\}$ is identified, where $e(s)$ denotes the sampled EEG, $u_j\Delta t = t((j\text{-}1)K + 1)$ $v_j\Delta t = t(jK)$, and $\Delta t = 1/256$ sec. Since EEG is a continuous time process recorded at a fixed sampling rate, the traditional Fast Fourier transform (FFT) is applicable. In this study, the FFT is calculated using the Welch windowing method in the MATLAB scientific package [88]. The spectral power in *theta*, *alpha* and *beta* bands are estimated and normalized by the total EEG signal power of the interval.

3.2   *Fractal Analysis of Signal Fluctuation*

While spectral analysis provides the signal decomposition in the frequency domain, it does not characterize the nature of the signal fluctuation. As mentioned in the introduction, the fluctuation in physiological data typically exhibits fractal property and multiple scaling. To capture such a property, it is necessary to employ singularity analysis in the time-domain.

3.2.1 Singularity Analysis

In general, the study of time series fluctuation has a very intuitive basis. Among others, the data fluctuation describes its "ability" of jumping from one value to the next. It is thus not surprising that the time-domain study of data fluctuation rests on the property of derivatives of the data viewed as a function. In technical terms, the study of function differentiability is called singularity analysis.

Let $x(t)$ be the data of interest. Treated as a function, its singular property can be measured by the so-called local Hölder exponent. Specifically, given $C(t) > 0$, $\alpha' > 0$, one can find an nth order polynomial $P_n(t)$, $n < \alpha$, such that, for $\delta < \delta_0$, the following inequality holds

$$\left| x(t+\delta) - P_n(t) \right| \le C|\delta|^{\alpha(t)} \tag{3.3}$$

The Hölder exponent of $x(t)$ is defined as the greatest exponent α for which (3.3) is valid. If $x(t)$ is n times continuously differentiable at t, $P_n(t)$ can be selected as the order n Taylor expansion of x at t and, therefore, $\alpha < n$. According to the above definition, it is clear that the larger $\alpha(t)$ is, the smoother the function becomes and, thus, the lesser the degree of fluctuation. Similarly, a small $\alpha(t)$ means strong fluctuation. Of particular interest is the range where $\alpha < 1$. It corresponds to a fluctuation that does not have a well-defined derivative. This particular exponent range applies to the RRi fluctuation in healthy humans. Note that α is a function of t. The range it covers also reveals important information about the fluctuation. The fluctuation characterized by a small α range implies "uniformity" in that the degree the time series fluctuates is more or less the same. However, if α covers a large range, the time series is said to be more *complex* where "mild" and "violent" fluctuations coexist, giving the appearance of strong intermittency.

3.2.2 1-D WTMM

It is also important to note that (3.3) is a point-wise definition. This allows the singular property to be studied as a function of scale. The natural tool to accomplish this is by the wavelet transform:

$$T_\psi[x](t,a) = \frac{1}{a} \int_{\infty}^{-\infty} \psi\left(\frac{t'-t}{a}\right) x(t') \, dt' \qquad (3.4)$$

In (3.4), $T_\psi[x](t,a)$ is called the wavelet coefficient of $x(t')$ at $t' = t$ and scale a, and $\psi(t)$ is called the analyzing wavelet. To capture local characteristics of $x(t)$, it is necessary that the analyzing wavelet vanishes everywhere except locally at $t = 0$ [89]. Hwang and Mallat [19] proved that the wavelet coefficient $T_\psi[x](t,a)$ displayed in the time scale plan (t, a) registers a very distinct geometrical feature depending on the differentiability of the function $x(t)$. In particular, it was shown that the singular property of a function is uniquely associated with the formation of the maxima of the modulus $|T_\psi[x](t,a)|$. Given a range of scales, these modulus maxima form the so-called *maxima lines*. Bacry et al. [18] showed that the exponent $\alpha(t)$ can be estimated effectively using the wavelet transform modulus value along these maxima lines $|T_\psi[x]|$.

There is a deeper structure in the set of Hölder exponent $\{\alpha\}$. Using WTMM, such a structure can be obtained by considering the analogy of the partition function in statistical physics. Specifically, let

$$Z(a,q) = \int \left|W[x](t,a)\right|^q dt, q \in \mathbb{R} \qquad (3.5)$$

Equation (3.5) is similar to the partition function of a statistical mechanical system with $\|W[x]\|$ being compared to the exponential of the energy state and q to the inverse of temperature

of the canonical ensemble, see [90]. Denote the set of maxima lines at scale a by $L(a) =$ $\{l_1, l_2, \ldots l_{N(a)}\}$. Bacry et al. [18] proved that

$$Z(a;q) = \sum_{l_i \in L(a)} C_i^q \sim a^{\tau(q)} \tag{3.6}$$

where $C_i = \sup_{(t,a) \in l_i} \left| T_\psi[x](t,a) \right|$ is the supremum of the modulus maxima along the maxima line l_i, for all scales less than a and $\tau(q)$ is called the scaling function. Bacry et al. [18] further showed that the Legendre transform of $\tau(q)$ yields the singularity spectrum $f(\alpha)$ of the support $\{t, \alpha(t) = \alpha\}$:

$$\tau(q) = \min_\alpha \left(q\alpha - f(\alpha) \right) \tag{3.7}$$

3.2.2   Joint WTMM

For this research, it is essential to analyze the joint fractal fluctuation of RRi and EEG. The WTMM-based partition function approach (3.5) and the subsequent Legendre transform (3.7) provide one of the most reliable and systematic framework to analyze the (infinite) fractal subsets in multifractal objects. To achieve the same for multiple time series, the WTMM was extended for fractal analysis of one time series and a joint WTMM approach was developed to estimate the fractal correlation in multiple time series. This extension has been found possible and can be carried out effectively [31].

Consider $x_k(t)$ where $k = 1, 2$ and their respective sets of singularity exponents $\{\alpha_k\}$. Let the maxima lines of $\left| T_\psi[x_k] \right|$ at scale a be denoted as $L_k(a)$, $k = 1, 2$. A natural extension of the existing WTMM analysis is to consider a joint partition function of the form:

$$Z(a;q,p) = \sum_j C_{1,r(j)}^q C_{2,s(j)}^p \tag{3.8}$$

23

where $C_{1,r(j)}^q, C_{2,s(j)}^p$ are the modulus maxima of the maxima lines $l_{1,r} \in L_1, l_{2,s} \in L_2$. To realize

(3.8), the maxima lines in L_k (a), $k =1,2$ must be paired up properly. The matching process is

outlined in a flowchart in Appendix C. As in correlation analyses, the objective here is to

characterize the property related to observing both singularity exponents α_1 and α_2 at a particular

given time and scale. In terms of WTMM, such information should be contained in the modulus

of the neighboring maxima lines. If the time coordinate of $l_{k,j}(a)$ is denoted by $t_{k,j}(a)$, this means

the coefficients $C_{1,r}$, $C_{2,s}$ paired up in (3.8) can be determined by

$$\left| t_{1,r} - t_{2,s} \right| = \min_{r'} \left(\left| t_{1,r'} - t_{2,s} \right| \right) = \min_{s'} \left(\left| t_{1,r} - t_{2,s'} \right| \right) \tag{3.9}$$

When (3.9) cannot be met, the same process is repeated recursively for the unpaired coefficients,

without any overlapping. Finally, the remaining unmatched coefficients are paired with a '0'

coefficient so that

$$\begin{aligned} Z(a;q,0) &= Z(a;q) \\ Z(a;0,p) &= Z(a;p) \end{aligned} \tag{3.10}$$

Note that these added '0s' will not affect the partition function value for $q, p > 0$. Figure 3-1 is a

visual illustration of (3.9).

Once (3.8) and (3.9) are established, the subsequent singularity analysis can follow the

1D case as developed by Bacry et al [18]. In particular, based on $C_{k,\lambda} \sim a^{\alpha_k(\lambda)}, \lambda = r, s, (3.8)$ can

be given by

$$\begin{aligned} Z(a;q,p) &\sim \sum_j a^{q\alpha_1(r(j)) + p\alpha_2(s(j))} \\ &= \iint d\alpha_1 d\alpha_2 P(\alpha_1, \alpha_2) a^{q\alpha_1 + p\alpha_2 - f(\alpha_1, \alpha_2)} \end{aligned} \tag{3.11}$$

24

where $P(\alpha_1,\alpha_2)$ and $f(\alpha_1,\alpha_2)$ are the joint probability density function and Hausdorff dimension of the support of (α_1,α_2), respectively. Applying the standard argument of steepest descent in small a yields

$$Z\big(a;q,p\big) \sim a^{\tau(q,p)} \qquad (3.12)$$
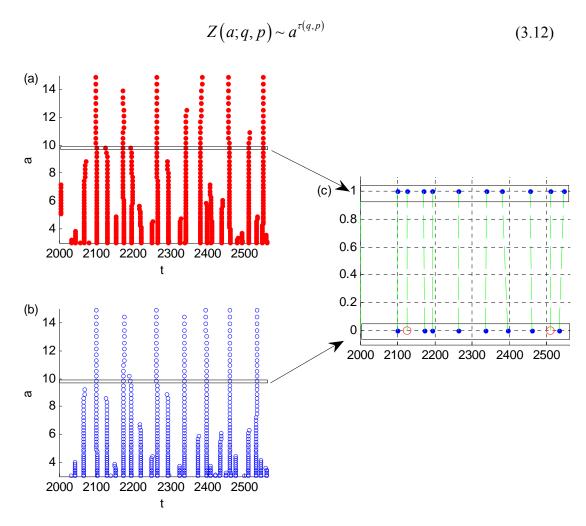
Figure 3-1 Pairing up of the WTMM coefficients. (a) Maxima lines of $C_{1,r}$ (b) Maxima lines of $C_{2,s}$ (c) Matched coefficients. Insertions of zeroes are denoted by empty circles and the dashed line shows the pairing of the coefficients.

where

$$\tau\big(q,p\big) = \min_{\alpha_1,\alpha_2}\big(q\alpha_1 + p\alpha_2 - f\big(\alpha_1,\alpha_2\big)\big). \qquad (3.13)$$

From (3.13), it is seen that $\tau(q,p)$ and $f(\alpha_1,\alpha_2)$ form a Legendre transform pair:

$$\alpha_1 = \partial \tau (q,p) / \partial q, \alpha_2 = \partial \tau (q,p) / \partial q_2,$$
$$f(\alpha_1,\alpha_2) = \alpha_1(q,p)q + \alpha_2(q,p)p - \tau(q,p)$$
(3.14)

where

$$q = \partial f / \partial \alpha_1, p = \partial f / \partial \alpha_2$$
(3.15)

The matlab code used to compute the JWTMM partition function is given in Appendix D.

3.3 Relative Multifractal Analysis

There are robust and accurate tools, [18, 91-93] such as WTMM, for estimating the fractal property of time series, however, there is relatively little work on the study of correlation between fractal objects. Part of the difficulty is that fractality is a property of the entire probability density function and therefore depends on the moment of all orders. This is in contrast to the traditional correlation measure that is defined by second order statistics. Another difficulty lies in the fact that the fractal subsets in multifractal object are "intertwined" in a highly nontrivial way and, thus, cannot be "singled out" directly for comparison from the time series.

The discussion of fractal correlation or a similar notion is not new. Essential to this idea is the distinguishability of the singularity spectra. At least for the class of multifractal process known as the cascade (see below), there is a positive answer in that no two multifractal spectrum $f(\alpha)$ can be exactly the same unless the underlying processes are generated by the same cascade [31]. However, the spectrum $f(\alpha)$ of a group of cascade processes can be made arbitrarily close to each other and, thus, cannot be distinguished in any finite precision device. For this reason, Levy-Lehel and Vojak [94] and Riedi and Scheuring [58] independently developed the ideas of using the singularity of one multifractal object to measure that of the other. Essentially, these authors provide the basis to measure the fractal correlation. The mathematical abstractions have

26

in fact an interesting link to the JWTMM technique introduced above. It turns out that the joint exponent $\tau(q,p)$ contains all the information about the fractal correlation developed by these authors. In this research, the setting known as the relative multifractality developed by Riedi and Scheuring [58] is mainly followed.

Consider multifractal measures π and μ. Assume that the generation of singularities in $\pi(\mu)$ is related to that in $\mu(\pi)$. To be specific, measuring the multifractal property of π using μ will be considered. It will be shown that it naturally fits into the framework of the joint partition function approach of (3.8) introduced in the last section.

First, recall the joint partition function of π is given by

$$\sum_{A \in H} \pi(A)^q \sim |A|^{\tau_\pi(q)}, \quad \sum_{A' \in H'} \mu(A')^p \sim |A'|^{\tau_\mu(p)} \tag{3.16}$$

where H, H' denote the generic partitions of the support and $|\cdot|$ denote the Lebesgue measure of the set. It is evident from (3.16), that the Lebesgue measure plays a fundamental role to measure the singularity. To examine the extent to which the singularity of π correlates with μ, the Lebesgue measure in (3.16) is replaced by using the second measure. For π measured by μ, one writes (after moving all to the left-hand-side)

$$\sum \pi(A)^q \mu(A)^{-t(q)} \sim O(|A|) \tag{3.17}$$

where the "big O" describes the order relationship $O(|A|) \rightarrow$ const. as $|A| \rightarrow 0$. Clearly $t = \tau_\pi$ when $\mu(\cdot) = |\cdot|$. Cole proved that there exists an upper bound, $\tau_{\pi/\mu} = \sup\{t(q)\}$, for which (3.17) holds [95]. Evidently, when μ is replaced by $|\cdot|$, one recovers the partition function of a single measure $\pi : \sum \pi^q \sim O(|a|) + a^{-\tau_\pi}$. Following the same framework as in the fractal analysis of one time series, one can similarly define the multifractal spectrum of π relative to μ, $f(\alpha_{\pi/\mu})$, via the Legendre transform of $\tau_{\pi/\mu}$, where $\alpha_{\pi/\mu}(q) = d\tau_{\pi/\mu}(q)/dq$. The interpretation thus follows, namely,

the relative multifractal spectrum $f(\alpha_{\pi/\mu})$ is a function that characterizes the support of the singular behavior of the form $\pi \sim \mu^{\alpha_{\pi/\mu}(q)}$.

To relate to the JWTMM technique introduced above, comparing (3.17) with (3.8) and (3.12) shows that $\tau_{\pi/\mu}$ can be obtained as the level set of $\tau(q, p) = 0$ where

$$p = -\tau_{\pi/\mu}(q) \tag{3.18}$$

Note that, by switching the role of q, p, the singular behaviour of μ can be gauged by π in a similar way. With the same arguments, one arrives at $\tau_{\mu/\pi}$ defined by the same level set $\tau(q, p) = 0$ where $q = -\tau_{\mu/\pi}(p)$. It may be useful to point out that $\tau_{\pi/\mu}$, $\tau_{\mu/\pi}$ on the $q \times p$ plane are nothing but mirror images of the level set $\{\tau(q,p) = 0\}$ about $p = 0$ and $q = 0$ axes, respectively.

While the approach using the partition function provides the framework to study joint fluctuation of multifractal objects, it does not go beyond the traditional multifractal analysis. Combined with relative multifractal analysis, it is now possible to reveal additional details. Hereafter, $\tau_{\pi/\mu}$ ($\tau_{\mu/\pi}$) will be called the common multifractal factor (CMF of $\pi(\mu)$ relative to $\mu(\pi)$. Given the CMF, the fractal correlation of fractal objects can be formally defined and characterized.

3.4 *Multifractal Correlation*

In this section, the fractal correlation based on the CMF defined above will be defined. In particular, the width spectrum of the CMF, $f(\alpha_{\pi/\mu})$, provides an effective parameter to measure the fractal correlation. First, consider a few important cases to motivate the idea. For identical $\pi = \mu$, it is intuitive that the referenced measure is viewed completely "uniform" by the referencing measure. As a result, one expects a simple monofractal type of scaling relationship. In this case, the joint partition function is simply a re-parametrization:

$$Z(a;q,p) = \sum \pi(I)^q \mu(I)^p = \sum \pi(I)^{q+p} \sim a^{\tau_\pi(q+p)} \tag{3.19}$$

i.e., $\tau(q, p) = \tau(q + p)$. By definition, $L(0) = \{(q, p), \tau(q, p) = 0\} = \{(q, p), \tau_\pi(q, p) = 0\} = \{q + p = 1\}$. Hence, the $L(0)$ is given by the straight line $q = 1 - p$, and $\alpha_A = 1$. Applying the Legendre transform, one has a degenerate or a monofractal description: $f(\alpha) = 1$ for $\alpha_A = 1$ and $f(\alpha) = 0$ elsewhere. In general α_A is bounded. For example $\alpha_{\pi/\mu}$ lies between α_π when $\mu = |\bullet|$ and $1/\alpha_\mu$ when $\pi = |\bullet|$. The former follows from the definition of the multifractal spectrum of π and the latter follows from (3.18) and the definition of the multifractal spectrum $f(\alpha_{\pi/\mu})$, via the Legendre transform of $\tau_{\pi/\mu}$ above.

From the "monofractal" CMF for $\pi = \mu$ to the more general case discussed above, it is evident that, the stronger the correlation between π and μ is, the narrower $f(\alpha_A)$ becomes and vice versa. Since CMF is derived from the same $L(0)$, this statement holds regardless of the "point of view," $A = \pi/\mu$ or μ/π. Thus, one can use the width of the multifractal spectrum of the CMF, $f(\alpha_A)$, to measure the multifractal correlation in jointly fluctuating scale-free processes.

$$W(I_q) = \max\left(\alpha_{\pi/\mu}(q)\right) - \min\left(\alpha_{\mu/\pi}(q)\right) \tag{3.20}$$

where $q \in I_q = [q_{min}, q_{max}]$. A smaller W would be associated with stronger multifractal coupling and vice versa [59].

Consider two CMFs $\tau^1_{\pi/\mu}$ and $\tau^2_{\pi/\mu}$. The functional difference can be used to quantify the difference in correlation between the CMFs.

$$\rho_p = \frac{\int_{I_q} \left|\tau^1_{\pi/\mu} - \tau^2_{\pi/\mu}\right| dq}{I_q} \tag{3.21}$$

where I_q is the interval of q where both the CMFs are obtained. Switching the role of q and p, another value for the functional difference can be obtained

$$\rho_q = \frac{\int_{I_p} \left| \tau^1_{\mu/\pi} - \tau^2_{\mu/\pi} \right| dp}{I_p} \qquad (3.22)$$

where I_p is the interval of p where both the CMFs are obtained. Numerically, ρ_p and ρ_q are not the same because I_q and I_p are different.

3.5   Aggregation

By embarking on the joint analysis of EEG and RRi, one must address the fundamental difference of the continuous-time EEG process and the discrete-time RRi process. To this end, the EEG is aggregated on a beat-to-beat basis so as to 'compare' with the RRi [96]. Let RRi and its time stamp be $r(n)$, $t(n) = \sum_{l=1}^{n} r(l)$, $n = 1, 2, ...,$ respectively. Let the selected EEG signal be $e(s)$, $s = \Delta t, 2\,\Delta t, ...$ and $\Delta t = 1/256$ sec, $e(s)$ is aggregated based on $t(n)$:

$$e_A(n) = \left(\sum_{t(n)}^{t(n+1)} e(s) \right) / (t(n+1) - t(n)) \qquad (3.23)$$

It is important to point out that the aggregation process (3.23) is not based on a fixed interval as done in the literature since $r(n) = t(n+1) - t(n)$, the beat-to-beat RR interval, fluctuates. Numerical tests conducted in the past indicate that the scaling property of $e(s)$ is still preserved in $e_A(n)$ within the normal range of $r(t)$ [60]. While the aggregation is necessary in order to achieve the joint multifractal analysis with RRi, it could have additional benefit of being able to reduce the effect from unwanted artifacts, such as scalp muscle twitch, that appears as uncorrelated chance artifact in EEG.

3.6   Numerical Experiment – Coupled Binomial Cascade

The coupled random binomial cascades studied by Meneveau et al. provide the most direct link between CMF and the multifractal correlation [57]. In this case, one can in fact go one step further to relate to the underlying generating mechanism.

Consider the random binomial cascade π, referred to as the π-cascade, generated by deterministic weights $p_0 \in [0, 1]$ and $p_1 = (1 - p_0)$. Let I_H, $H = h_1, \ldots h_j$ denote the interval generated in the jth level construction where $h_i \in \{0,1\}$ and $\sum h_i 2^{-i}$ is the based-2 coarse-grained representation of any $x \in I_H$. By definition, $\pi(I_H) = \prod_{j=1}^{J} p_{h_j}$. Now consider a second binomial cascade μ, referred to as the μ-cascade, generated by weights m_0, m_1 and $\mu(I_S) = \prod_{j=1}^{J} m_{r_j}$, $S = s_1, \ldots s_j$. With the same addressing scheme, one can write the value of μ –cascade as $\mu(I_H)) = \prod_{j=1}^{J} m(h_j)$.

To couple the cascades, a parameter g and a uniform random variable γ in $[0,1]$ are used. Let I_L, I_H be the offspring intervals created in the construction of the cascades. If $\gamma < g$ the weights assigned to I_L, I_H for the μ-cascade will depend on exactly how the weights of the π-cascade are assigned. In particular, if p_0 is assigned to I_L (I_H) of the π-cascade, m_0 will be assigned to I_L (I_H) of the μ-cascade and similarly for p_1 and m_1. If $\gamma > g$ the weight assignment for the cascades will be completely independent from each other. This way, the fractal generating mechanisms of the cascades are completely dependent on each other when $g = 1$, and independent of each other when $g = 0$. When the cascades are completely dependent, it is expected that the singularities of π and μ will arise at exactly the same instant in time. When the cascades are generated independently, this coincidence is no longer valid. Numerical tests on various g values have been conducted and reported in a journal publication [31].

31

For the numerical experiment, 30 sets of data, each for $g = 0, 0.3, 0.8, 1$ were generated. The range of q used in the partition function was limited from -4 to +4 with increments of 0.5. A typical realization for $g = 0.3$ is shown in Figure 3-2. The first order Gaussian wavelet was used in the JWTMM outlined above to obtain the CMF. Typical maxima lines of the coupled cascades are shown in Figure 3-3.
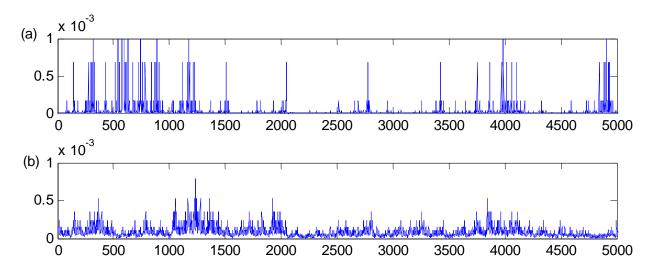
Figure 3-2 Coupled binomial cascade for $g = 0.3$. (a) $p_0 = 0.2$, $p_1 = 0.8$ and (b) $m_0 = 0.4$, $m_1 = 0.6$.

It is observed that the maxima lines are "organized" as expected: namely, they are mostly "aligned" when the fractal generation is completely dependent at $g = 1$ and begin to "mis-align" for $g < 1$. The systematic change of the maxima lines imply changes in the CMF in these cases, which results in the different width estimate of the corresponding $f(\alpha_A)$ spectrum. This is demonstrated below, along with using the functional distance method.

The joint partition functions are shown in Figure 3-4 (a). The power law scalings are found in all cases. The corresponding $\tau(q,p)$ is shown in Figure 3-4 (b).
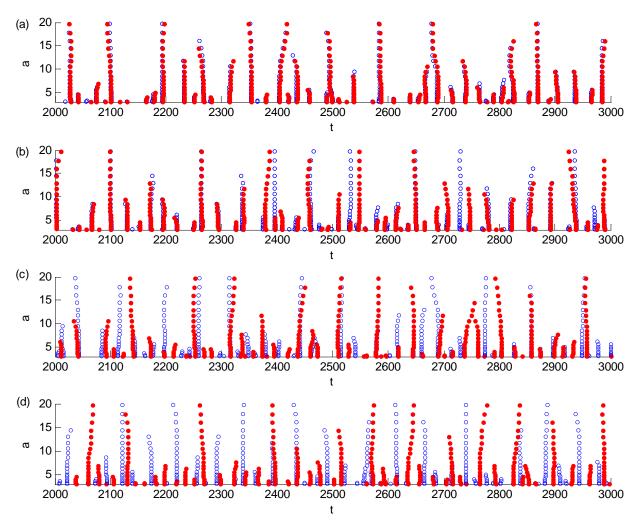
Figure 3-3 Typical maxima lines from the π- (blue " $\bigcirc$ ") and μ-cascades (red " $\bullet$ ") with coupling parameter $g = 1.0, 0.3, 0.8, 0.0$, (a) – (d) respectively.
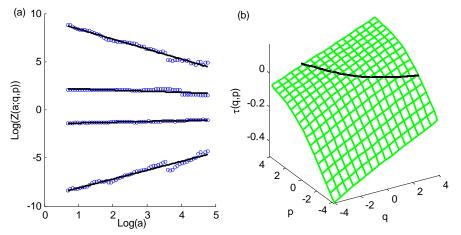
Figure 3-4 The joint partition function Z and the joint scaling exponent τ of coupled binomial cascades with $g = 0.3$. (a) Power law trend of the joint partition function $Z(a,q,p)$. The fitted slopes are shown by the solid lines for $(q,p) = (-1,1.5), (3.5,-1.5), (0.5, 0.5), (-1, 3.5)$ from top to bottom. (b) $\tau(q,p)$, the black line corresponds to $L(0)$.

33

The averaged $\tau_{\pi/\mu}$ for each g value is shown in Figure 3-5(a). It is seen, as $|q|$ gets larger, that the $\tau_{\pi/\mu}$ for different g begins to deviate from each other systematically. Their Legendre transform is shown in Figure 3-5(b).

It is seen that the numerical results follow the reasoning in section 3.4 and show that a stronger coupling between the cascades leads to a curvier $\tau_{\pi/\mu}$, and consequently, a narrower width of the $f(\alpha_{\pi/\mu})$ Figure 3-6(a). The example demonstrates how the width of $f(\alpha_{\pi/\mu})$, $W(I_q)$ can be a useful indicator for the multifractal correlation in jointly fluctuating multifractal objects.
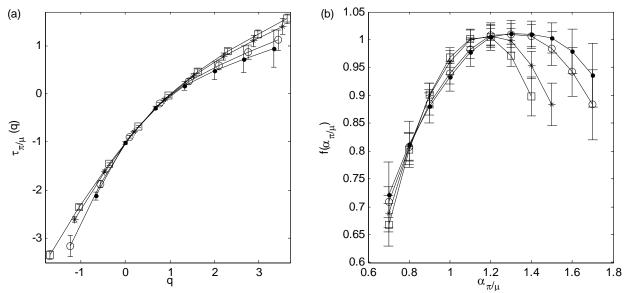
Figure 3-5 (a) $\tau_{\pi/\mu}$, "•", "○", "*", "□" correspond to $g = 0$, 0.3, 0.8, and 1 respectively. (b) $f(\alpha_{\pi/\mu})$ of the same cascades in (a).

To compute the functional difference (3.21) and (3.22), two binomial cascades without a random variable forming a completely dependent cascade such that $g = 1$, were created. The resulting $\tau_{\pi/\mu}$ was used as a reference to compute ρ_p and ρ_q and are shown Figure 3-6 (b) and (c). Both ρ_p and ρ_q metrics increase as the difference between the cascades increase.
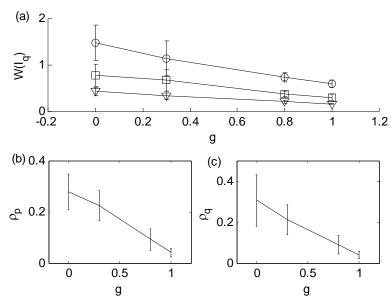
Figure 3-6 (a) $W(I_q)$, $I_q = [0.3,-0.3]$ ("Δ"), [0.5, -0.5], ("□") and [1,-1] ("○"). (b) ρ_p, (c) ρ_q for coupled binomial cascades

Chapter 4   The Central Component and HRV in HUT – Frequency-Domain Assessment

In this chapter, the result from the frequency domain approach applied to the fluctuation of RRi and EEG data is given. The main advantage of the frequency domain approach is the known physiological correlates of the RRi and EEG spectral properties that can provide the preliminary interpretation and reference for the results of this research.

For the heart rate, changes in the LF range of the RRi are generally regarded as a quantitative marker for both SNS and PNS activities, and the HF component can be related to mainly the PNS activity [11, 82]. The origin of the LF component has been suggested by the "baroreflex resonance" hypothesis [97]. In this explanation, the LF originates from the so-called Mayer waves, when the baroreceptors sense blood pressure changes, which results in the subsequent ANS modulations on the circulatory system. These modulations undergo a 180º phase shift at the frequencies of approximately 0.1 Hz because of the delay characterizing neural modulations of peripheral resistances. This is believed to form a positive feedback loop, underlying the oscillation [98].

The origin of the HF component of RRi has been less controversial than the LF component. In particular, it is largely believed to reflect PNS activity. Among others, the HF component in short-term recording also characterizes the important respiratory sinus arrhythmia resulting from the interaction between respiration and SNS activity [99]. In the controlled breathing protocol, RSA is more pronounced and is typically manifested in the narrow band characteristics of the HF range in the RRi frequency spectrum. In spontaneous breathing, where subjects are allowed to breath at his/her own pace and is used in the current protocol, the property of RSA for medium to long RRi record is less noticeable due to the power law broad band background of the spectrum [35]. According to the Task Force document by the European

Society of Cardiology and the North American Society of Pacing and Electrophysiology [11], the range [0.04, 0.15] Hz is considered to cover the LF range and [0.15, 0.4] Hz to the HF range.

For the EEG data, there is a large volume of literature on the characterization of its frequency contents and the underlying cognitive functions; see the excellent book by Niedermeyer [71]. The reference to the states of alertness and relaxation that are likely provoked by the HUT maneuver are relevant to the current research. The specific frequency components in connection to these brain states have been identified by the so-called *delta*, *alpha* and *beta* rhythms.

The *alpha* band is perhaps the most well-known of all. It is roughly defined in the [8,13] Hz of the frequency spectrum of EEG and is more pronounced when taken in the parieto-occipital, occipital areas of the scalp [72]. The signal power in the *alpha* band was found to be reduced in the eyes open state and upon the presentation of visual stimuli [100-102, 102]. The neural origins of these oscillations have in fact been demonstrated by recordings at the cellular level [103]. Enhanced *alpha* rhythm has also been recorded during mental tasks in the frontoparietal network [104]. Recent studies have suggested the *alpha* state is more active than previously thought [105]. Furthermore, the origin of oscillations in the alpha band has been linked to thalamic-occipital interactions [Gomez].

Beta band activity is largely identified with the primary motor cortex, where oscillations involve pyramidal neurons projecting to the spinal cord. These oscillations are coherent with similar oscillations in corticomuscular recording, and are abolished during movement [106]. The function of *beta* band activity remains unclear, but recently it has been suggested that it is involved in sensorimotor integration [107]. It is generally associated with normal waking consciousness [108].

Theta band activity originates from the cortico-hippocampal interactions [109]. *Theta* band activity in the hippocampus has been linked to mnemonic processes and spatial information processing. Aftanas et al. [110] reported persistent increase in *theta* band power during the presentation of emotional stimuli that induced sympathetic activation.

4.1 Relative EEG-ANS index

To capture potential CNS, ANS interactions in the HUT maneuver, a new variable to measure the change in the frequency contents of one nervous system relative to the other is introduced as the relative EEG-ANS index.

Specifically, recall that the RRi and EEG data are first segmented, and the signal power of *r(n)* in LF, and HF are estimated using the Lomb method and the signal power of EEG (*P*) is estimated using the FFT (section 3.1). Let G = UPR or SUP, hereafter. As mentioned above, there is SNS activation and PNS withdrawal after the HUT maneuver. This can be characterized by the so-called sympatho-vagal index defined as

$$A_{LF/HF}^{G}(j) = P_{LF}^{G}(j) / P_{HF}^{G}(j) \tag{4.1}$$

Recall from section 3.1, that *j* refers to the segment number. The HUT effect measured by the ANS activity alone is thus described $A_{LF/HF}^{UPR} > A_{LF/HF}^{SUP}$. To characterize the CNS response under ANS perturbation, for *b = theta, alpha, beta*, and for *d =* LF, HF, LF/HF, the ratio of EEG spectral power and RRi spectral power as a relative EEG-ANS index is calculated:

$$R_{b,d}^{G}(j) = P_{b}^{G}(j) / A_{d}^{G}(j) \tag{4.2}$$

where $A_{LF}^{G} = P_{LF}^{G}$ and $A_{HF}^{G} = P_{HF}^{G}$. Since the HUT effect in ANS results in $A_{LF/HF}^{UPR} > A_{LF/HF}^{SUP}$, $R_{b,LF/HF}^{UPR}(j)$ tends to be small. A systematic change in $R_{b,d}^{UPR}$ relative to the control in SUP implies CNS-ANS interaction and the potential CNS influence in HRV. In this research, the

increment of the averaged $\left\langle R^G_{b,d} \right\rangle = \sum_j R^G_{b,d}(j) / N_K$ is used to characterize the HUT effect from

the two nervous systems:

$$T_{b,d} = \left\langle R^{UPR}_{b,d} \right\rangle - \left\langle R^{SUP}_{b,d} \right\rangle \tag{4.3}$$

A $T_{b,d} \sim 0$ implies a large EEG-ANS index in UPR as a result of a strong CNS response

under the ANS perturbation and vice versa.

4.2   Results

The RRi and EEG data from a typical subject are shown in Figure 4-1. In Figure 4-2, the

normalized spectral powers P, of EEG and RRi for a typical subject are shown as they vary with

each segment. It is clear that $A^{UPR}_{LF/HF} > A^{SUP}_{LF/HF}$, which characterizes the expected increase of the

sympatho-vagal index in HUT. This realization holds for all the subjects, indicating the full

effect of SNS activation and PNS withdrawal from the HUT maneuver (Table 3).

Figure 4-3 shows the EEG – ANS indices $R^G_{b,d}(j)$ for S6. Given the EEG-ANS index, the

$T_{b,d}$ was calculated according to (4.3) for the same subject. To search for an indication of the

central influence, a scatterplot was constructed and the subsequent regression analysis was

conducted for $T_{b,d}$ for different $b,\ d$ combinations. After a systematic comparison, the

combination involving the *theta*, *beta*, bands and *theta*, *alpha* reveals the strongest statistically

significant correlation based on the regression fits and $p < 0.01$ see Figure 4-4(f), (g), (i) and the

corresponding correlation coefficient and p values in Table 4.
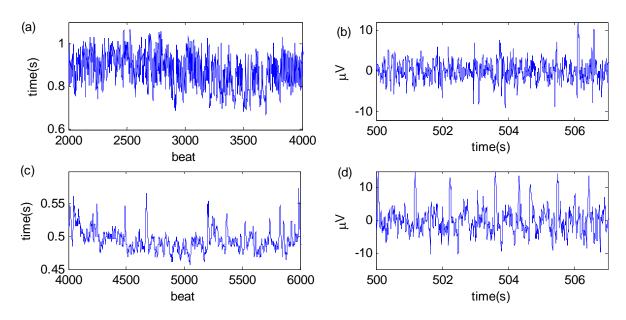
Figure 4-1 Data Segments from S6. (a) RRi during SUP, (b) EEG during SUP, (c) RRi during UPR, (d) EEG during UPR.

Figure 4-2 Normalized EEG spectral power of S6. (a) P_{LF}^{UPR} (black) and P_{LF}^{SUP} (blue), (b) P_{theta}^{SUP}, (c) P_{theta}^{UPR}, (d) P_{HF}^{UPR} (black) and P_{HF}^{SUP} (blue), (e) P_{alpha}^{SUP}, (f) P_{alpha}^{UPR}, (g) $A_{LF/HF}^{UPR}$ (black) and $A_{LF/HF}^{SUP}$ (blue), (h) P_{beta}^{SUP}, (i) P_{beta}^{UPR}. The horizontal red lines are their respective means.

40

Table 3 Spectral Components of EEG and sympathovagal index for all subjects

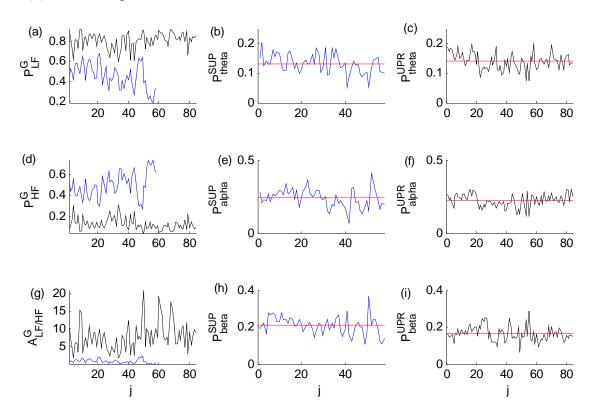|	A		P_{theta}		P_{alpha}		P_{beta}	
	SUP	UPR	SUP	UPR	SUP	UPR	SUP	UPR
S1	1.17±0.78	3.61±2.1	0.139±0.025	0.099±0.025	0.345±0.067	0.173±0.046	0.225±0.032	0.243±0.06
S2	0.608±0.37	9.89±5.4	0.17±0.04	0.101±0.064	0.314±0.068	0.129±0.057	0.216±0.034	0.355±0.12
S3	3.02±1.4	12.9±4.8	0.197±0.039	0.204±0.037	0.203±0.044	0.235±0.04	0.194±0.038	0.176±0.038
S4	2.27±0.99	3.63±1.6	0.13±0.02	0.0867±0.015	0.109±0.06	0.0747±0.041	0.0534±0.033	0.0699±0.047
S5	0.723±0.53	13.6±5.7	0.138±0.028	0.164±0.024	0.478±0.056	0.389±0.057	0.155±0.033	0.161±0.028
S6	1.03±0.52	7.86±4	0.132±0.032	0.14±0.027	0.238±0.065	0.222±0.043	0.209±0.048	0.162±0.04
S7	2.51±1.3	7.36±4.2	0.194±0.054	0.137±0.032	0.272±0.14	0.537±0.055	0.155±0.078	0.109±0.016
S8	0.966±0.67	1.47±0.68	0.193±0.071	0.173±0.034	0.47±0.13	0.332±0.058	0.126±0.023	0.206±0.025
S9	1.21±0.51	14.4±6.5	0.141±0.036	0.183±0.037	0.517±0.1	0.393±0.078	0.141±0.043	0.168±0.031
S10	0.58±0.31	9.85±6.3	0.214±0.03	0.236±0.028	0.259±0.03	0.273±0.033	0.215±0.038	0.209±0.019
S11	1.12±0.41	8.54±3.7	0.158±0.041	0.148±0.032	0.279±0.1	0.353±0.099	0.253±0.08	0.201±0.044
S12	1.17±0.42	12.6±5.7	0.161±0.027	0.105±0.035	0.353±0.063	0.295±0.082	0.175±0.034	0.231±0.049
S13	0.477±0.21	1.27±1.2	0.0261±0.0059	0.222±0.031	0.0465±0.011	0.14±0.022	0.121±0.028	0.171±0.021

$$T_{theta,HF} \sim T_{alpha,HF} \tag{4.4}$$

$$T_{theta,LF/HF} \sim T_{beta,LF/HF} \tag{4.5}$$

$$T_{theta,LF/HF} \sim T_{alpha,LF/HF} \tag{4.6}$$

It is important to note that the reference to $A^G_{LF/HF}$ is necessary to achieve the "data collapse" for (4.5). For example, the regression analysis shows a significant drop in correlation coefficient from $r = 0.8$ to $r = 0.05$ when using only the increment of the EEG spectral component T_b vs $T_{b,LF/HF}$. It is also important to point out that the $A^G_{LF/HF}$ trend does not directly translate into some of the linear trend observed above. These results derived from (4.4) ~ (4.6) have in fact a very specific meaning in the context of multifractal HRV. This is shown in the next chapter using the joint multifractal analysis.
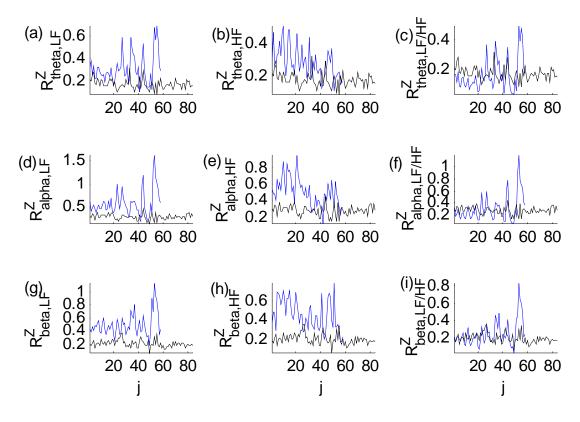
Figure 4-3 $R^{SUP}_{b,d}$ (blue) and $R^{UPR}_{b,d}$ (black) for S6. (a) $R^G_{theta,LF}$, (b) $R^G_{theta,HF}$, (c) $R^G_{theta,LF/HF}$, (d) $R^G_{alpha,LF}$, (e) $R^G_{alpha,HF}$, (f) $R^G_{alpha,LF/HF}$, (g) $R^G_{beta,LF}$, (h) $R^G_{beta,HF}$, (i) $R^G_{beta,LF/HF}$
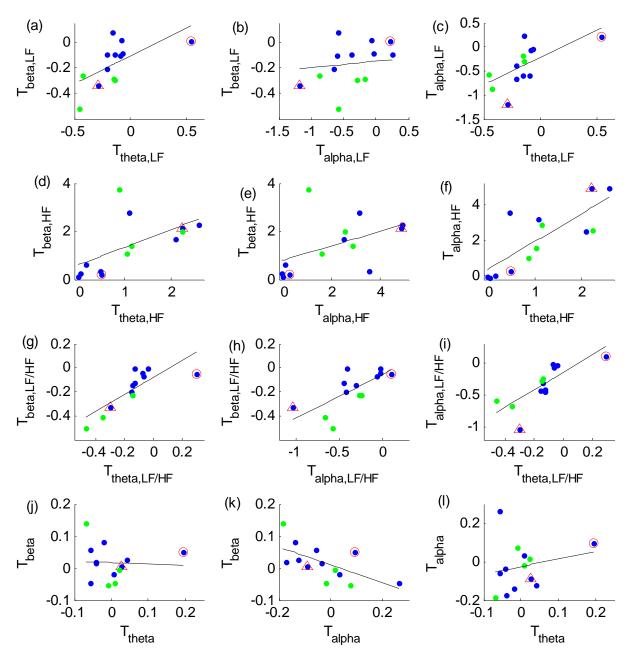
Figure 4-4 Scatterplot of correlation relationships. S2, S6 S10 and S11 (green "•") and the rest (blue "•"). S5 (red "Δ") and S13 (red 'o') are marked separately. The regression line coefficients are shown in Table 4.

Table 4 Regression lines and correlation coefficients for Figure 4-4

Figure 4-4	Regression line	Correlation coefficient r, (p)
(a)	y = -0.9x + 0.04	0.62 (0.02)
(b)	y = 1.2x -0.18	0.47 (0.66)
(c)	y = 0.4x	0.65 (0.02)
(d)	y = 0.5x + 0.4	0.59 (0.03)
(e)	y = 0.75x + 1	0.47 (0.10)
(f)	y = 0.4x + 0.3	0.79 (0.00)
(g)	y = 0.9x + 0.02	0.80 (0.00)
(h)	y = 1.4x − 0.086	0.71 (0.01)
(i)	y = 0.4x + 0.01	0.78 (0.00)
(j)	y = -0.07x	0.05 (0.86)
(k)	y = -1.5x	0.64 (0.02)
(l)	y = 0.1x	0.22 (0.47)

Chapter 5   The Central Component in HRV – Time-Domain Assessment

In this chapter, the potential central component of the fractal HRV is studied using the time domain fractal analysis. The fractal behavior of RRi has also been investigated under the autonomic perturbation of HUT. Based on short term RRi recordings, Butler et al. reported a decrease in fractal dimension using the power law spectrum exponent [63, 111]. More recently, similar results have been provided using detrended fluctuation analysis [112, 113]. Given its multifractal nature, [114] these results only describe one (among infinite) scaling exponent in HRV and did not describe the full scope of multifractal HRV in HUT. Nevertheless, they imply that a qualitative change of the multifractal HRV takes place under the autonomic perturbation of HUT.

Scale-free property in EEG recordings has been reported in both humans [115-119] and animals [120]. EEG recorded during epileptic seizures has been reported to be multifractal [121]. The scale-free characteristics of EEG were found to vary between individuals, age [122], qualitatively different brain states, between the REM and non-REM sleep [123], and exhibit self-organized criticality in the switching dynamics between the EEG background fluctuation and (narrow band) *alpha* rhythm in healthy humans [105].

Given the extensive integration between ANS and CNS in the higher brain centers, it is plausible that the autonomic perturbation from HUT can induce variation in the multifractal HRV dynamics. Based on this premise, the objective of this chapter is to use time domain fractal tools to find clues of such a central influence. Specifically, a novel technique was developed to extract the common multifractality among time series showing fractal fluctuation. Evidence that

the question of a central multifractal connection can be answered affirmatively in the current HUT maneuver will be presented.

5.1   Singularity Analysis

In this section, separate analyses of the fractal property of RRi and EEG are given using WTMM as described in section 3.2.1. These results not only provide a rough classification of the signals, they also serve as an important reference for the joint multifractal analysis given in section 5.2 below.

The RRi $r(n)$, EEG, $e(s)$ and the aggregated EEG $e_A(n)$ (3.23) from a typical subject are shown in Figure 4-4 below.

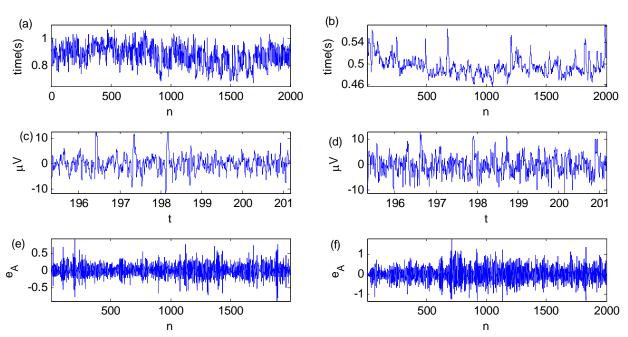**Figure 5-1** Data segments from S6. (a) RRi SUP, (b) RRi UPR, (c) EEG SUP, (d) EEG UPR, (e) Aggregated EEG SUP, (f) Aggregated EEG UPR.

The fractal properties of $r(n)$ and $e_A(n)$ are analyzed using the WTMM approach described in Chapter 3. The 3rd 4th and 5th Gaussian wavelets were used as the analyzing wavelet. These different Gaussian wavelets yielded only minor differences. In this section, the

46

results based on the 4th order Gaussian derivative wavelet for $r(n)$ and the 3rd order Gaussian wavelet for $e_A(n)$ will be presented. The range of q was limited to $[-2, 2]$ with increments of 0.05.

Figure 5-2 shows the typical wavelet modulus maxima lines of $r(n)$ for S6. The multifractal spectra $f(\alpha)$ of $r(n)$ for all the subjects are shown in Figure 5-3. The wavelet modulus maxima lines of $e_A(n)$ of the same subject is given in Figure 5-4. The multifractal spectra $f(\alpha)$ of $e_A(n)$ for all the subjects are shown in Figure 5-5.
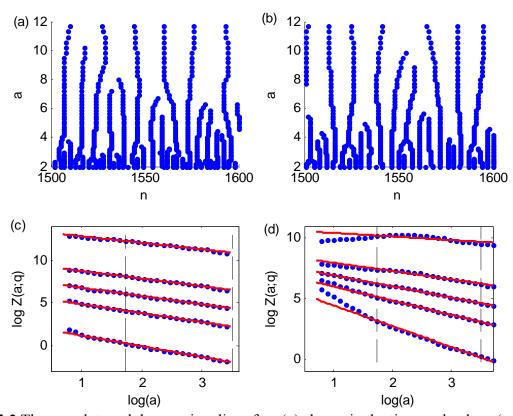
Figure 5-2 The wavelet modulus maxima lines for $r(n)$ shown in the time scale plane (n,a) for S6 in (a) SUP, (b) UPR. Scaling plot of the partition function $Z(a;q)$ in (c) SUP and (d) UPR. The fitting ranges are bounded by the vertical dashed lines and the fitted slopes are shown by the solid red lines for $q = 1.5, 0.5, 0 -0.5, -1.5$ (top to bottom).

Figure 5-3 $f(\alpha)$ of RRi in SUP, (blue " o"), and UPR ("red +") for subjects S1 ~ S13 in (a) ~ (m), respectively.


Figure 5-4 The wavelet modulus maxima lines for $e_A(n)$ shown in the time scale plane (n,a) for S6 in (a) SUP, (b) UPR. Scaling plot of the partition function $Z(a;q)$ in (c) SUP and (d) UPR. The fitting ranges are bounded by the vertical dashed lines and the fitted slopes are shown by the solid lines for $q = 1.5, 0.5\ 0, -0.5, -1.5$, top to bottom.
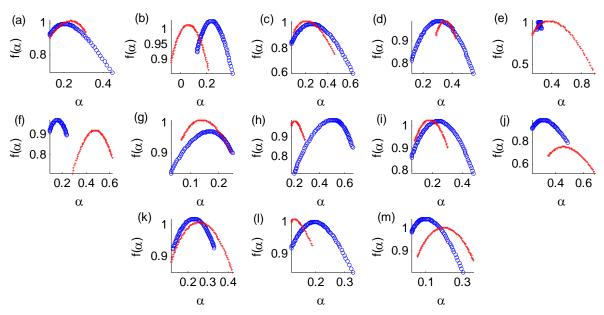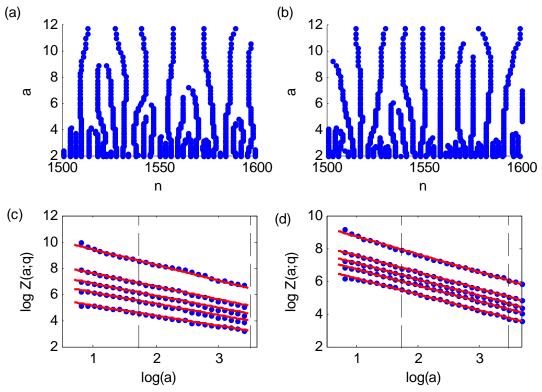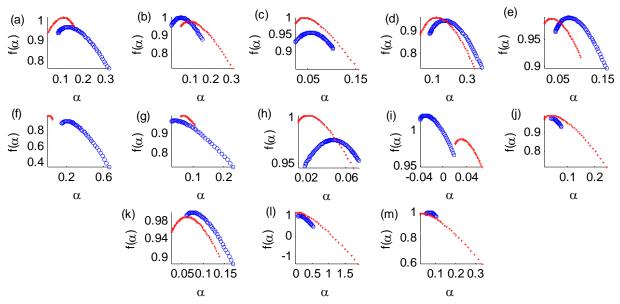
Figure 5-5 $f(\alpha)$ of e_A, in SUP (blue " o"), and UPR (red "+") for subjects S1 ~ S13 in (a) ~ (m), respectively.

It is important to observe that, even with the expected SNS activation and PNS withdrawal in the current HUT maneuver, the $f(\alpha)$ spectra of $r(n)$ do not show a systematic trend going from SUP to UPR. These spectra suggest that SNS and PNS activities may represent only two of many "degrees-of-freedom" of the multifractal HRV dynamics. This observation is also significant since the $f(\alpha)$ spectrum of $r(n)$ can be systematically altered by using particular chemical compounds to dampen the neurotransmission of ANS (such as atropine for PNS blockade and beta-blocker for SNS blockade). The missing of a systematic trending behavior indicates that the multifractal HRV has a different expression when both the SNS and PNS branches are active.

To characterize the HUT effect, the finite width of $f(\alpha)$, $W^G_{EEG}(I_q)$, $W^G_{RR}(I_q)$, $q \in I_q = [q_{min}, q_{max}]$, G = UPR or SUP, is calculated. According to the definition (Chapter 3), a large α exponent interval means more complex fluctuation given by a wide range of singularity strengths. Thus, one can use these width estimates to define a complexity index

$$U_v = W_v^{UPR}(I_q) / W_c^{SUP}(I_q) \qquad (5.1)$$

where $v = e_A$ or RRi. Equation (5.1) provides a convenient interpretation of the HUT effect: when $U_v > 1$, the current HUT maneuver results in a transition towards increased multifractal complexity, and vice versa.

Figure 5-6 shows the U_{e_A} and U_{RRi}. Note that due to the limited time that a HUT test can be performed, the full width of $f(\alpha)$ cannot be obtained. The ratio U_v given above is found to be robust varying slightly with the I_q interval except for the S5 in Figure 5-6(a), and S3, S12, S13 in Figure 5-6(b). Note that for S5, S12 and S13, there is no qualitative change in U_v, which remains greater than 1. Five subjects (S2, S5, S6, S10, S11 and S13) had $U_{RRi} > 1$, meaning a shift to more multifractal complexity for RRi with tilt. The remaining subjects indicate a transition to a narrower $f(\alpha)$ or reduced multifractal complexity. Five subjects (S2, S10, S11, S12, and S13) had $U_{e_A} > 1$, meaning a shift to more multifractal complexity in EEG.
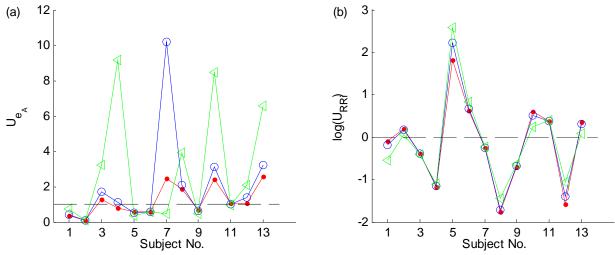

Figure 5-6 (a) U_{e_A} and (b) log(U_{RRi}). For $I_q = [-0.5,0.5]$ (red "•"), $I_q = [-1,1]$ (blue " o"), and $I_q = [-2,2]$ (green "△").

5.2   Relative Multifractal Analysis and Multifractal Correlation

The comparisons made above are based on separate multifractal analyses of RRi and EEG data. Such a comparison can be made rigorous for certain processes in theory. However, different fractal structures can yield very similar appearance and makes such comparisons practically impossible due to finite resolution [31]. For this reason, it is important to employ the joint multifractal analysis and relative multifractality concept to directly analyze the fractal elements in multiple data sets (Chapter 3). The goal for this section is to present the results that describe the relative multifractality and fractal correlation between RRi and EEG.

As described in Chapter 3, the joint multifractal analysis can be carried out using the JWTMM technique. To this end, the aggregated EEG and RRi were first integrated (Section 3.2.2). JWTMM was then applied using the first and second order Gaussian derivative wavelets. Higher order Gaussian derivative, Daubechies family and Coiflet family wavelets were compared against the first and second order Gaussian derivative wavelet [31]. They were found to lead to more fluctuation in $Z(a;q,p)$ and subject the estimation of $\tau(q,p)$ to more statistical error for large negative moments q_1 and q_2. At the present time, the author does not have any further insight as to why the lower order Gaussian derivative wavelet yields better results in JWTMM. In this dissertation, the results based on the first order Gaussian derivative wavelet are reported. The range of q, p are both limited to $[-3, 3]$ with every increment of 0.2.

The maxima lines and the scaling of the joint partition function from a typical subject are shown in Figure 5-7. Using the fractal property of $e_A(n)$ to measure the fractal property of $r(n)$, one arrives at the CMF, $\tau_{R/E}$, and the corresponding $\alpha_{R/E}, f(\alpha_{R/E})$ (section 3.4). These results from S6 are given in Figure 5-8.
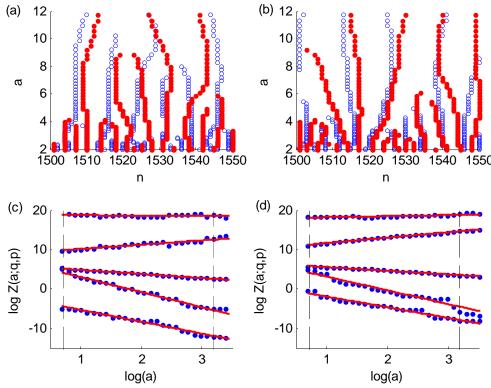
Figure 5-7 The wavelet modulus maxima lines for $r(n)$ (blue " o"), and $e_A(n)$ (red "•") shown in the time scale plane (n,a) for S6 in (a) SUP, (b) UPR. Scaling plot of the partition function $Z(a;q,p)$ in (c) SUP and (d) UPR. The fitting ranges are bounded by the vertical dashed lines and the fitted slopes are shown by solid lines for $(q,p) = (-2,2), (2,2), (0,0),(2,-2),(-2,2)$ from top to bottom.

In Figure 5-9, $\tau_{R/E}$ for all the subjects are shown. It is important to note that the $\tau_{R/E}$ for S2, S6, S10, and S11 are almost flat implying a narrow $f(\alpha_{R/E})$. This observation will be revisited shortly.

5.2.1 Multifractal Correlation

To characterize the HUT effect, the same idea of estimating the complexity index used in section 5.1 is followed. Specifically, denote the width of the Hölder exponent $\alpha_{R/E}$ in SUP, UPR, by $W_{R/E}^{SUP}(I_q)$ and $W_{R/E}^{UPR}(I_q)$. Figure 5-10(a) shows the results based on $I_q = [-2\ 2]$. The smallest values of the width $W_{R/E}^{UPR}(I_q)$ are for the same group of subjects identified previously in

Figure 5-8 Multifractal factorization result from S8. (a) $\tau(q,p)$ SUP, (b) $\tau(q,p)$ UPR. The black line in (a) and (b) is the location of $L(0)$, (c) $\tau_{R/E}$ SUP (d) $f(\alpha_{R/E})$ SUP (e) $\tau_{R/E}$ UPR and (f) $f(\alpha_{R/E})$ UPR.

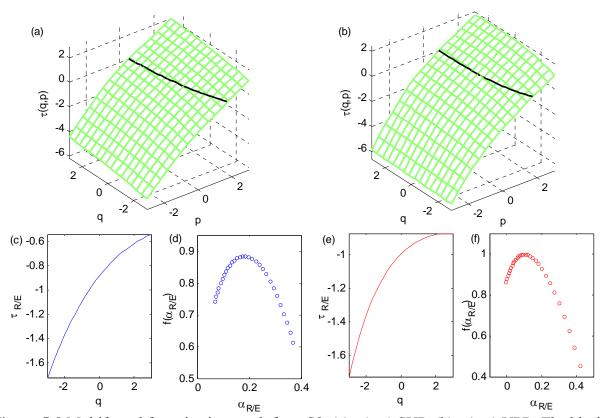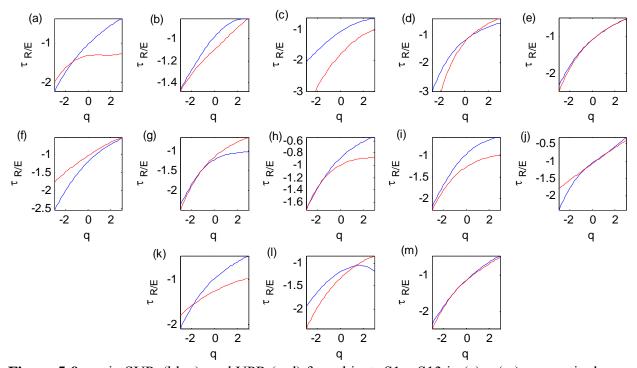**Figure 5-9** $\tau_{R/E}$ in SUP, (blue), and UPR (red) for subjects S1 ~ S13 in (a) ~ (m), respectively.

Figure 5-9, S2, S6, S10 and S11. This is expected since these subjects have a rather flat $\tau_{R/E}$, which implies more monofractal-like property.

From the same idea of complexity index used in section 5.1, consider the ratio of the width estimate of $f\left(\alpha_{R/E}\right)$ in UPR and SUP, $U_{R/E} = W_{R/E}^{UPR}\left(I_q\right) / W_{R/E}^{SUP}\left(I_q\right)$. Based on the interpretation given in section 3.4.2, the width and the multifractal correlation have a reciprocal relation. Hence, a large $U_{R/E} > 1$ implies the transition towards more multifractal complexity from SUP to UPR. Shown in Figure 5-10(b) are the complexity index of all the subjects based on the CMF calculation for I_q = [-2 2], [-1 1], and [-0.5 0.5]. Due to their small $W_{R/E}^{UPR}(I_q)$, S2, S6, S10, S11 also have a small $U_{R/E}$ and thus exhibit a stronger multifractal correlation in UPR compared to SUP.

This result shown in Figure 5-10(b) has an interesting parallel to the multifractal HRV given in Figure 5-6. As shown earlier, these same subjects also experienced increased HRV multifractal complexity from SUP to UPR. Two other subjects S5 and S13 shown in Figure 5-6 also exhibited increased HRV multifractal complexity from SUP to UPR but did not match the parallel as these other four subjects. However, it should be noted that the health issues of S5 are
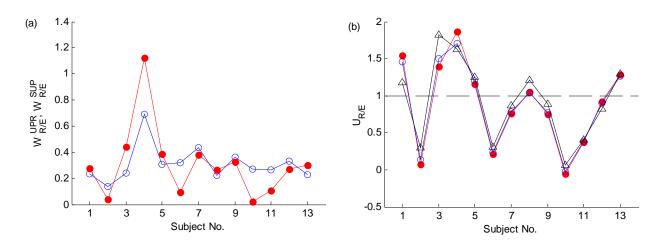
Figure 5-10 $f(\alpha_{R/E})$ results. (a) $W_{R/E}^{UPR}$ (red "•") and $W_{R/E}^{SUP}$ (blue "o"), I_q = [-2, 2] (b) $U_{R/E}$, I_q = [-0.5, 0.5], (red "•"), I_q = [-1, 1], (blue "o"), I_q = [-2, 2] (black "Δ").

mentioned in Chapter 2 and that S13 is likely an outlier with higher than usual *theta* power (Figure 4-4). This subject also indicated sleepiness during the tilt test.

5.2.2 Functional Distance

In this section, the results based on the functional distance (3.31) between $\tau_{R/E}$ in SUP and UPR are presented. The result of a typical subject (S3) is shown in Figure 5-11. It is observed that the ρ_q and ρ_p yields very different results from the $U_{R/E}$. In contrast to the case of binomial cascades shown in Figure 3-6(b) and (c), there is no consistency between ρ_q, ρ_p and $U_{R/E}$. A closer look at the $\tau_{R/E}$ (Figure 5-9) and that of the binomial cascades (Figure 3-5) reveals the issue of normalization.

Since the cascades were normalized to satisfy the condition of a probability measure, i.e., $\sum \mu = \sum \pi = 1$, there is, however, no such constraints imposed on the experimental data. In that light, it should be mentioned that the fractal correlation estimate $W_{R/E}^{G}$ is based on the derivative of CMF, and is not influenced by the issue of normalization.

Figure 5-11 Functional distance $\tau_{R/E}$ of S3 measured from (a) common q intervals, (b) common p intervals. The shaded region is where the functional norm is taken. (c) ρ_q for all 13 subjects based on (a). (d) ρ_p for all 13 subjects based on (b).

55

5.3   Surrogate Data Analysis
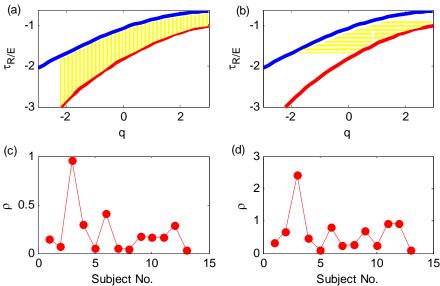
The multifractal correlation results should be shown to be "particular" and to not describe chance events. To this end, RRi and aggregated EEG surrogates are constructed and the results compared. Similar to a test of statistical significance, the surrogate analysis describes a systematic method to examine whether the observed property is genuine or a coincidence [124]. In this work, two algorithms were used to create surrogate data, random permutation (shuffle) and the iterated amplitude adjusted Fourier transform (iAAFT) method. They are first described in the following section and then analyzed by using the same procedure for the original data.

5.3.1 Construction and Singularity Analysis

Let $x(t)$ be the data of interest. The shuffled surrogate is achieved by simply reordering $x(t)$ along the time axis via random permutation. This results in removing any existing correlation in the data. For every $r(n)$, $e_A(n)$ collected in SUP and UPR, 55 sets of randomly permutated RRi $r_s(n)$ and aggregated EEG $e_{As}(n)$ were generated. Typical realizations of $r_s(n)$ based on S6 in SUP are shown in Figure 5-12 (a) and (b). The PSD of these surrogates are shown in Figure 5-13 (a) and (b). The appearance of the flat power spectrum indicates that the correlation in the data has been completely destroyed by the shuffling process.

The amplitude adjusted Fourier transform (AAFT) method was derived based on the hypothesis that the non-Gaussian distribution is not a result of the system characteristics, but rather a manifestation of the measurement system [125]. The actual observation is thus a composition of the 'distortion' from the measurement and the original data; i.e., $s(x)$ was observed, rather than $x(t)$. The objective of AAFT is to build an alternative version of the observed data $s(x)$, x_{pr}, which preserves all the underlying properties except that the amplitude

56

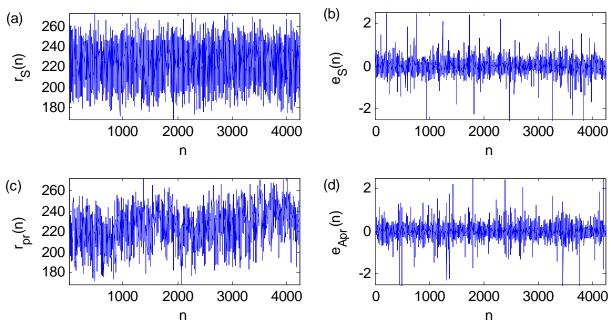**Figure 5-12** Surrogate data created from S6. (a) $r_{As}(n)$ in SUP, (b) $e_{As}(n)$ in SUP, (c) $r_{pr}(n)$ in SUP, and (d) $e_{Apr}(n)$ SUP.
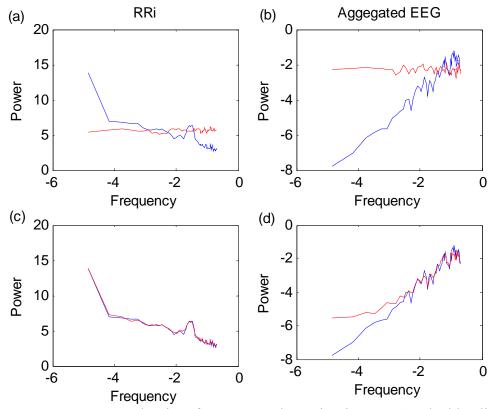

Figure 5-13 Power spectrum density of surrogates shown in Figure 5-12. The blue line is the PSD of the original data, and the red line is the PSD of the surrogates. (a) $r_S(n)$ from SUP, (b) $e_S(n)$ from SUP, (c) $r_{pr}(n)$ from SUP, and (d) $e_{Apr}(n)$ from SUP.

57

distribution of x_{pr} being 'restored' to the Gaussian form. It is an attempt to invert the observation $s(x)$ by rescaling the data into a Gaussian distribution. However, the procedure is biased to a flatter spectrum since the inverse of $s(x)$ is not available [124]. The iterated AAFT (iAAFT) allows the adjustment of the spectrum and amplitude distribution to be made iteratively[126]. To summarize, the iterative procedure can be given in the following 7 steps:

1) Obtain the squared amplitudes of the Fourier transform of $x(t)$, X_k^2, $k = 1,2,..$

2) Create a random permutation of $x(t)$, x_s^0.

3) Create the inverse Fourier transform, x_s^i for $i = 1$, from the original squared amplitudes X_k^2 but keeping the phase from x_s^{i-1}.

4) Rank order x_s^i according to $x(t)$.

5) Obtain the squared amplitude of the Fourier transform of x_s^i, $X_{k,i}^2$.

6) Calculate the difference, $d_i = X_{k,i}^2 - X_k^2$.

7) Repeat step 3 to 6 for $i = 2, 3…$ until $d_{i+1} >= d_i$.

The final iteration produces a surrogate x_s^i with a randomized phase and a similar PSD. For this method, 55 sets of iAAFT RRi $r_{pr}(n)$ and aggregated EEG $e_{Apr}(n)$ are also generated.

An example from a typical subject is shown in Figure 5-12 (c) and (d). The PSD of the iAAFT surrogates are shown in Figure 5-13 (c) and (d). For the $r_{pr}(n)$, it is clear that the surrogate exhibits a similar PSD. The PSD of $e_{Apr}(n)$ shows the flatness bias in the lower frequency part of the spectrum associated with earlier methods [124] still exists with aggregated EEG. This is because d_i does not converge to 0 in the numerical method and further iteration does not cause a change in the values of x_s^i.

5.3.2 Relative Multifractal Analysis

All the surrogates are processed based on the same data analysis procedure for the original data. The range of q, p are both limited to $[-3, 3]$ with increments of 0.2. The maxima lines and the scaling of the joint partition function from S6 are shown in Figure 5-14. The CMF associated with $e_{As}(n)$ and $r_{As}(n)$, $e_{Apr}(n)$ and $r_{Apr}(n)$ are shown Figure 5-15, for the same subject.
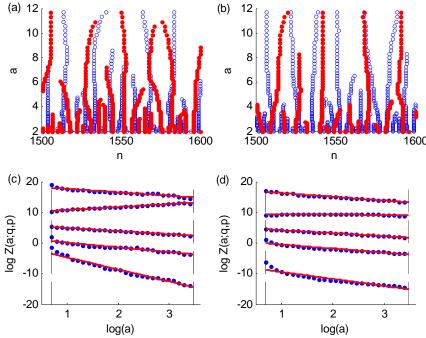
Figure 5-14 The wavelet modulus maxima lines for $r(n)$ (blue "o"), and $e_A(n)$ (red "•") shown in the time scale plane (n,a) for S6 surrogates in (a) SUP shuffled, (b) UPR iAAFT. Scaling plot of the partition function $Z(a;q,p)$ in (c) SUP and (d) UPR. The fitting ranges are bounded by the vertical dashed lines and the fitted slopes are shown by the solid lines for $(q,p) = (-2,2)$, (2,2), (0,0),(2,-2),(-2,2) from top to bottom.

For all the shuffled surrogates, the corresponding $W_{R/E}^{SUP}$ and $W_{R/E}^{UPR}$ were found to be lower compared to the original data as shown in Figure 5-16 (a) and (c). It shows a drastic contrast to the results of the original data (blue " o" and red "•"). As reviewed in section 5.3.1, iAAFT differs from random permutation by conserving the PSD. The resulting $W_{R/E}^{SUP}$ and $W_{R/E}^{UPR}$ from the iAAFT surrogates are not as uniform as the shuffled surrogates as shown in Figure 5-16 (b) and (d). However, the iAAFT surrogate does not follow the same trending behavior as the original

data (blue " ∘" and red "•"). This suggests that the fractal correlation observed in Figure 5-10 is
likely to be a genuine property of the underlying data.
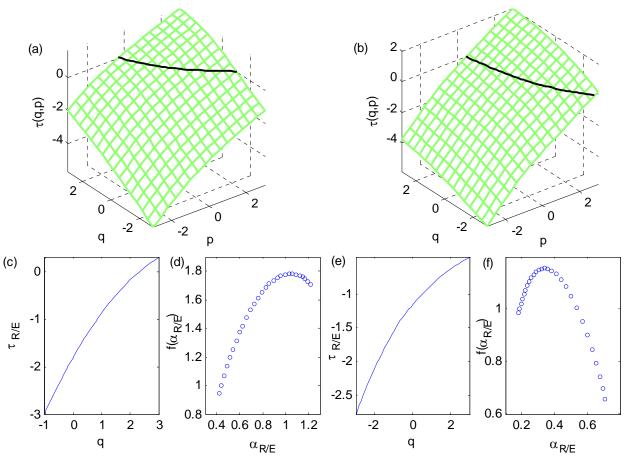
Figure 5-15 Multifractal factorization result from S6 surrogates. (a) $\tau(q,p)$ from shuffled surrogate SUP, (b) $\tau(q,p)$ from iAAFT surrogate SUP, (c) $\tau_{R/E}$ from shuffled surrogate SUP, (d) $f(\alpha_{R/E})$ from shuffled surrogate SUP, (e) $\tau_{R/E}$ from iAAFT surrogate SUP, and (f) $f(\alpha_{R/E})$ from iAAFT surrogate SUP.
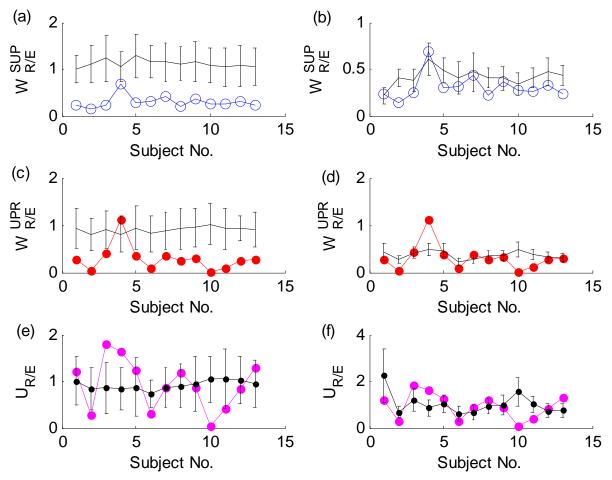
Figure 5-16 $f(\alpha_{R/E})$ results from surrogate data. Error bars are the standard deviation of the surrogates, SUP (blue " ○"), UPR (red "•"). (a) $W_{R/E}^{SUP}$ from shuffled data, (b) $W_{R/E}^{SUP}$ from iAAFT data, (c) $W_{R/E}^{UPR}$ from shuffled data, (d) $W_{R/E}^{UPR}$ from iAAFT data, (e) $\log(U_{R/E})$ from shuffled data, (f) $\log(U_{R/E})$ from iAAFT data. In (e) and (f), the error bars are the standard deviation of surrogates, and $U_{R/E}$ from original data (magenta "•").

Chapter 6   Discussion and Conclusion

The main result of this research is the evidence of a central component that varies with HRV multifractal complexity. To the best of the author's knowledge, the central influence on the multifractal property of HRV has not been described before. In this chapter, the current research findings are reviewed and discussed. Their implications are offered and limitations are noted. Finally, the conclusion and future research are given in the last section.

6.1   Discussion of Results

Based on the sympathovagal index $A_{LF/HF}^{Z}$ (Table 3), it is clear that all the test subjects experienced the HUT effect of SNS activation and PNS withdrawal [68, 127]. However $A_{LF/HF}^{Z}$ did not completely capture the qualitative features of the subjects' HRV multifractal complexity (Table 3). In contrast, the fractal correlation results provide a better parallel with the multifractal HRV property. Specifically, a closer examination of Figures 5-6(b) and 5-10(b) reveals that S2, S6, S10, and S11 had an increase in RRi multifractal complexity in UPR posture and a clear increase in multifractal correlation, as seen from the smaller width estimate of their $f(\alpha_{R/E})$. Similarly S1, S3, S4, and S8 had a decrease in RRi multifractal complexity after tilt and a decrease in multifractal correlation. Discounting the 2 subjects who revealed additional medical conditions after the test (see below), it was found that, in 8 out of 11 subjects, the increased (decreased) HRV multifractal complexity is correlated to a stronger (weaker) CNS-ANS multifractal correlation under the ANS perturbation of HUT. The consistent grouping of these subjects, one by the CMF based on EEG and RRi fluctuation and one by the RRi data, suggests a central-autonomic component in the HRV multifractal dynamics. In addition, judging from Figure 5-6, where no apparent relationship between the multifractality of RRi and aggregated

EEG can be found, it can be inferred that it is necessary to analyze the heart rate and brain data together in a multivariate approach. The main finding described above can further be supported by the results of the surrogate and spectral measures.

The two types of surrogates used in this research continue to exhibit multifractality (Figure 5-15). This is consistent with the current literature [128]. However, the width estimates of the $f(\alpha_{R/E})$ of the RRi and EEG surrogates are clearly different. In particular, the width estimates of the fractal correlation between shuffled surrogates are similar among all subjects. They suggest the surrogates have a qualitatively different behavior compared to the original data.

The unique characteristics captured by the fractal correlation measure were also present in the spectral increment analysis defined by the ratio of the EEG and HRV spectral components. In particular, the subgroup S2, S6, S10, S11 can once again be singled out. While showing strong central-autonomic fractal correlation, the spectral increments of this group are also more pronounced than the rest (Figure 4-4(g)), suggesting the potential link between the effect from UPR posture on the underlying multifractal complexity and central-autonomic fractal correlation.

To the best of the author's knowledge, there is little work on the multifractal HRV in HUT. The current approach differs from the literature by considering the multifractal spectrum with infinite scaling exponents. The HRV fractal property conducted in the past considered only one scaling exponent, such as the scaling exponent of the $1/f$ power law spectrum of RRi or the scaling exponent derived from the detrend fluctuation analysis see eg. [129] and references therein. Based on the fractal dimension defined by the power law spectral exponent of RRi, a number of studies reported a decrease of the fractal dimension in HUT [111-113, 130, 131], implying the transition towards a "simpler" fluctuation pattern. However, the fractal dimension so defined is a monofractal approach, which is not consistent with the multifractality in HRV. As

given in Figure 5-6(b), it is shown that it is in fact possible to have a range of multifractal "behavior." Tulppo et al. reported relative constant HRV complexity in HUT using the approximate entropy measure [128]. However, approximate entropy is defined to characterize the overall irregularity of the signal, including an unstructured random noise component [132]. The current approach using fractal correlation targets *only* on the scale-free component of the fluctuation and appears to better describe the underlying HRV scale-free dynamics.

The spectral analysis offers other interesting insights based on some of the known physiological correlates. Among the EEG spectral increments themselves (without dividing the HRV spectral indices), the *theta*, *beta* bands (Figure 4-4 (j)) and *theta*, *alpha* bands (Figure 4-4 (l)) are poorly correlated. Only the spectral increments between the *beta* and *alpha* bands show a significant negative correlation (Figure 4-4 (k)). The reciprocal change of these two EEG characteristics was also observed in healthy subjects who underwent mental tasks with increased SNS activity [133]. This is an intuitive interpretation since the *beta* band activity characterizes mostly cognitive processing and intense concentration, whereas the *alpha* band characterizes the opposite mental state of calm and relaxation. During HUT, there is an increase of alertness [130], which could contribute to the negative correlation between these two EEG bands. However, when normalized by the HRV spectral LF, HF components, the correlation between the *beta*, *alpha* spectral increments is much less significant than the other pairs, suggesting a weaker central-autonomic association with these two EEG bands.

In contrast, the normalized spectral increments are significantly correlated when the *theta* band is involved. As mentioned above, S2, S6, S10, S11, who exhibit the stronger fractal correlation in the group ($U_{R/E} \ll 1$), can once again be singled out in the corresponding spectral increment relationships. For example, this subgroup of subjects is immediately identified from

the $T_{theta\ LF/HF}$ and $T_{beta,LF/HF}$ relationship (Figure 4-4 (g)), followed by, after discounting subject S5 (see below), the $T_{theta,LF/HF}$ and $T_{alphs,LF/HF}$ relationship (Figure 4-4 (i)). There is some evidence that could support the present findings. Postural change to UPR has been shown to result in increased attention span and altered EEG *theta* band activity [85, 87]. These studies are consistent with the presence of the *theta* band in these relationships. In addition, Cole [134] has noted the increase of EEG *beta* band activity along with SNS activation in HUT, which supports the *beta* band activity in the present finding.

Given the distinct reactivity from the group, S2, S6, S10, S11, it is tempting to find clues to relate the subjects' characteristics to the findings reported in this thesis. Some similarity among the subjects was found showing transition towards increased HRV multifractal complexity and multifractal correlation from SUP to UPR: S2, S10, S11 are all trained athletes, representing various university sport teams. As part of their training routines, they were required to undergo endurance training. The effects of athletic training on the ANS control of the heart rate has been studied extensively in the past decades [135, 136], and are known to have different HRV fractal property [137]. Among the subjects showing transition towards decreased HRV multifractality with increased multifractal correlation, S7 and S12 reported that they meditate regularly. However, the reported negative correlation between *theta* band activity and SNS activity [138] and positive correlation with PNS activity [139] were not seen in this study. Subject S5 reported that he had undergone surgery requiring anaesthesia two days prior to the experiment. This subject went through the test without giving any prior notification. The subject was also under medication during the tests. This subject's data were included for completeness. Subject S13 reported some "irregular heart rhythm" diagnosed in the past but the arrhythmia was

not considered significant. It should be noted that these two subjects were the only two who exhibited increased HRV multifractal complexity with reduced multifractal correlation[2].

6.2   Limitations of the current study

A number of limitations exist in the design of the experiment. The number of subjects in the study is small. Increasing the number of subjects should provide better statistics to the present findings. Although the largest time scale of the analysis is limited by the length of time that the tilt test can be performed, for a typical test of 1 hour, it translates into a low frequency cut-off at 0.00028Hz which falls into the ULF range. In this case, the results are not expected to be affected by this intrinsic factor. However, the length of time that the test can be performed does influence the number of heart beats collected, which in turn affects the q-interval used to estimate the width of $f(\alpha_{R/E})$. As with most fractal tools, this is because fractal correlation analysis relies on estimating a statistical measure to characterize the power law of the joint partition function. From that respect, it is desirable to extend the time of the test. However, it is conceivable that a prolonged HUT test can introduce additional psycho-physiological factors that are difficult to assess. This point will be elaborated in the Conclusion and Future work below.

Except for subjects S5 and S13, who revealed existing medical conditions before the test, the relationship between the central-autonomic fractal correlation and HRV multifractal complexity applies to 8 of the remaining 11 subjects. The HRV fractal property is also known to vary with age [14-16] and is reportedly different male and female [140, 141]. It is plausible that these fundamental characteristics of HRV could have specific implications to the current findings. Whether the current result applies to broader demographics remain to be seen.

---

[2] Subjects S5 and S13 were not included in the technical results reported in the Journal.

It is also of note that different breathing patterns can lead to different HRV fractal pattern [70, 142, 143]. One of the main considerations in the experimental design for the current research was to "facilitate" the fractal dynamics. In general, it is considered undesirable to provoke any particular rhythmic pattern that may disrupt the CNS and ANS reactivity. In particular, it was reported significantly different cardiac-respiratory phase synchrony during the REM (less synchrony) and non-REM (more synchrony) stages of the sleep [144]. This suggest breathing pattern can be an important variable in the investigation of central-autonomic fractal correlation with HRV. Moreover, controlled fixed-pace breathing may induce relaxation, which could potentially solicit certain rhythmic pattern in the EEG data. It is for these reasons that spontaneous breathing was considered more adequate to achieve the "free running" protocol for the current research objectives.

6.3 Implications

In a recent HUT study, repeated measurements of HRV did not yield reproducible fractal exponents [145]. Furthermore, there is no consensus in the literature on what a "healthy" scaling exponent should be [13, 146]. The previous models of HRV complexity did not examine the role of the central-autonomic coupling. As a result, such issues as irreproducibility reported in the literature pose a direct challenge to the validity of these models [147]. The current finding provides a logical and intuitive explanation that the mechanism underlying the central-autonomic coupling could hold the key for HRV complexity. Changes in the dynamical state of the brain may affect the central-autonomic coupling, and lead to differences in HRV fluctuation.

The degree of variability in biological data has been deemed fundamental to the proper functioning of the underlying biological system. Hence, the current finding could provide the basis for further investigation between scale-free HRV and cardiovascular health. A weaker

central-autonomic coupling, which is found to correlate with reduced HRV multifractal complexity, may have implications on the "simpler" HRV pattern witnessed in certain heart disease processes. The precise origin of multifractal complexity within the CNS was not explored in this study. Further research with human models is necessary to characterize their precise connection.

The development of the novel technique JWTMM to measure the CMF allows the simultaneous fractal correlation analysis of multiple fractal signals. As mentioned in the introduction, scale free fluctuation is abundant in nature. In some systems, multiple variables have been shown to exhibit scale free fluctuations and this technique can be extended to study the fractal correlation between them. For example, in hydrodynamic turbulence this technique can be potentially extended to study the fractal correlation between dissipation of kinetic energy and vorticity.

6.4 Conclusion and Future Work

In this study, it was shown that the CNS modification in terms of the cortical neuronal activity measured by the EEG can have a direct expression in the multifractal HRV complexity. To the best of the author's knowledge, this is the first study to uncover the effect. In addition the data seem s to suggest that the theta band can play a significant role leading to a stronger central-autonomic coupling after HUT. Although this research does not address a causal relationship, the CMF result and its parallel with the transition of HRV multifractal complexity in HUT imply the paradigm which depicts a HRV model, not as predominantly described in the framework of ANS activity, but as a dynamical system driven by the overall nervous system.

The results of this work lead to some possible avenues of future research. New experiments should be designed to investigate the effects of physical activity and meditation on

central-autonomic coupling. Experiments that consider the changes in the central-autonomic coupling of at risk or diseased individuals may have diagnostic value in medicine.

Additional protocols can be considered such as controlled breathing and eyes closed state. These modifications are likely to add a different type of perturbation to the ANS, and would further facilitate the study of CNS influence on scale-free HRV.

Appendices

Appendix A   Consent form and Questionnaire

RYERSON UNIVERSITY

CONSENT FORM

I hereby accept to participate in a study on monitoring electrical activity in the brain and the heart associated with various motor and mental tasks. The procedures are completely non-invasive. I will not personally benefit from participating in these tests.

The tests require measurements of electrical activities of my heart and muscles with small non-invasive surface electrodes. The procedure is neither painful nor dangerous. I may feel minimal discomfort during preparation of the skin with alcohol, before the taping of the electrodes to the skin.

The study also requires measurements of electrical activities of my brain and muscles with small non-invasive surface electrodes. The procedure is neither painful nor dangerous. I may feel minimal discomfort during skin preparation or cleansing with a pumice paste before I wear an electrode cap, on which the screw-able surface electrodes are mounted.

I am asked to participate in one or more tests which are conducted while sitting and/or on a tilt table with foot rest. The tilt table test will progressively tilt my body from the supine to almost upright positions. I have been given detailed instructions and relevant physiology regarding all the tests.

I understand that I will receive no monetary compensation or any benefits for my participation.

If at any time I wish to stop participating in the experiment, I am free to do so. I understand that any questions that I may have about this study and my participation in it can be posed to Dr. D. Lin 416-979-5000 x 7489 (derlin@ryerson.ca).

At the end of the experimental session, if I would like to learn more about these experiments, I can further the discussion with the investigators the rationale, methods and observations, as well as the potential utilities and implications of this research.

I will also be given a copy of this consent form to keep.

_____   _____
                Witness   Date

Emergency Contact information:_____

_____
        Signature of Participant

Interview Questionnaire

Please answer the following questions briefly but accurately. You can choose not to answer (please indicate).

1) Do you meditate? If so, how long have you been meditating?

2) Do you have any known allergies to metals or other materials? We will apply gel and attach electrodes to your scalp to measure the electrical activity in your brain.

3) Have you been taking any medication on a long-term basis? If so, please briefly explain its effect.

4) Do you have any known neurological disorder?

5) Do you have a history of, or recently diagnosed, heart problems and high blood pressure?

6) Have you had any experience of syncope during a pro-long period in upright position? Please go back as early as you can to your best ability.

Before-Test Questionnaire

Please answer the following questions to the best of you abilities:

1) Recall your sleeping patterns for the last two days.

	Day – 1	Day – 2
Wake up time		
Sleep time (light off)		

2) Did you consume more than your usual amount of coffee, or nicotine (cigarettes, cigars etc) in the past 2 days? Also, is there any stress factor that you can identify, such as an upcoming test, or a significant event?

3) Did you drastically increase your physical activity in the past 2 days, such as joining a sport club, or start a new physical training?

4) Have you been taking any drug/medication in the past few days?

5) Please provide the following information:

Age: _____ Sex: ☐ M / ☐ F Height: _____ Weight: _____

Signature _____ Date _____

Appendix B   Lomb Method

Let $x(t)$ be the data of interest. The coefficients that represent $x(t)$ after transformation are

$$c_i = \int x(t) f_i(t) \, dt \qquad\qquad (A.1)$$

where $f_i(t)$ is the basis set of the Fourier transform. The square error is defined as

$$e(c_i) = \int \left(x(t) - c_i f_i(t) \right)^2 dt \qquad\qquad (A.2)$$

Minimization of (A.2) in its discrete form for unevenly sampled data, $x(t_n)$ leads to the

minimization of:

$$\sum \left| x(t_n) - c(i) f_i(t_n) \right|^2 \qquad\qquad (A.3)$$
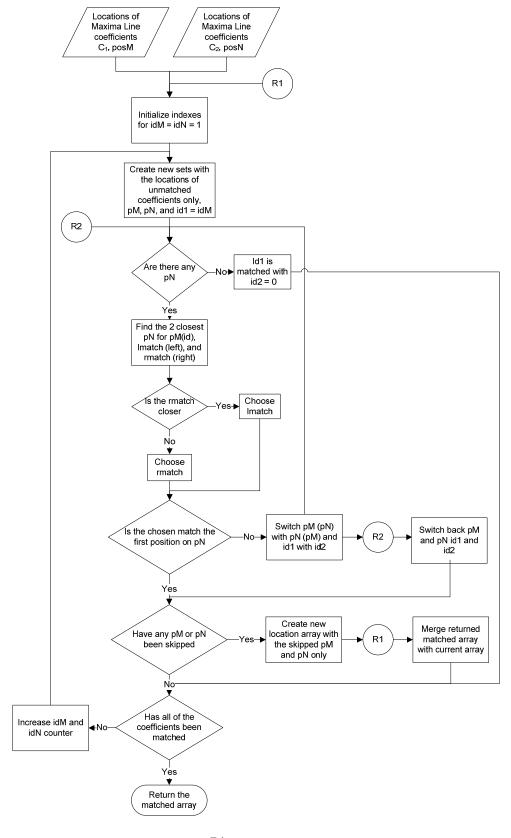
which results in

$$c_i = \frac{\sum x(t_n) f_i^*(t_n)}{\sum \left| f_i(t_n) \right|^2} \qquad\qquad (A.4)$$

where f_i^* is the complex conjugate f_i. This is known as the generalized Lomb method. Subsequently the signal power is defined as

$$P_i = c_i \sum x^*(t_n) f_i(t_n) \qquad\qquad (A.5)$$

Appendix C   Pairing of WTMM Coefficients

Appendix D   JWTMM Matlab Code

```matlab
function [pf,lscal] = jmmpf(x,y,ig, q,p, indx)


% This function computes the joint multifractal measure as outlined by
% Lin et al. (2007). x and y are the outputs of multifractal2.c, and q and
% p are the moments. The multifractal spectra of x is given by a(q,0), and
% the multifractal spectra of y is given ap(0,p).
% indx contains the index of all the good data without cutoff, e.g. [1 20;
% 25 50; 80 100] means that data from 1 to 20 is good, 25-50 is good,
% 80-100 is good and so on.




[M,pM,scal,mwbox] = wtmm(x,length(x),ig);
[N,pN,scal,mwbox] = wtmm(y,length(y),ig);
[nscal, npt] = size(M);

indx(:,1) = indx(:,1) + mwbox;
indx(:,2) = indx(:,2) - mwbox;

nq = length(q);
np = length(p);
sf = zeros(nq,np,nscal);
lscal = log(scal);

for iscal = 1:nscal
    coeff1 = null(1);
    coeff2 = null(1);
    for i = 1:size(indx,1);
        Midx = find(pM(iscal,:)>indx(i,1) & pM(iscal,:)<indx(i,2));
        Nidx = find(pN(iscal,:)>indx(i,1) & pN(iscal,:)<indx(i,2));
        [tcoeff1,tcoeff2,posarr] =
matchcoeffs(M(iscal,Midx),pM(iscal,Midx),N(iscal,Nidx),pN(iscal,Nidx));
        coeff1 = [coeff1 tcoeff1];
        coeff2 = [coeff2 tcoeff2];
    end

    for iq = 1:nq
        for ip = 1:np
            tmp = coeff1.^q(iq).*coeff2.^p(ip);
            id = find(~isinf(tmp)& tmp~=0 & ~isinf(log(coeff1)) &
~isinf(log(coeff2)) );
            sf(iq,ip,iscal) = sum(tmp(id));
            mu = tmp(id)./sf(iq,ip,iscal);
            pf(1,iq,ip,iscal) = sum(mu.*log(coeff1(id)));
            pf(2,iq,ip,iscal) = sum(mu.*log(coeff2(id)));
            pf(3,iq,ip,iscal) = sum(mu.*log(mu));
            pf(4,iq,ip,iscal) = log(sf(iq,ip,iscal));
        end
    end
end
```

```matlab
% *************************************************************

function [coeff1, coeff2, posarr]=matchcoeffs(M, posM, N, posN)
%Take out the zeros at the end of the rows
coeff1 = null(1);
coeff2 = null(1);
posM = posM(find(posM ~= 0));
posN = posN(find(posN ~= 0));
% setting up the matched position array
posarr = matchpos(posM,posN);
nposarr = size(posarr);
%matching the coefficients
for i = 1:nposarr(2)
    if (posarr(1,i)==0)
        coeff1(i) = 0;
    else
        coeff1(i) = M(posarr(1,i));
    end
    if (posarr(2,i)==0)
        coeff2(i) = 0;
    else
        coeff2(i) = N(posarr(2,i));
    end
end


function [stats]= getstats (pf, nq, np, lscal);

%Getting the slope and fstat, stored in stats
for i = 1:3
    for ip = 1:np
        for iq = 1:nq
            ytmp = squeeze(pf(i,iq,ip,:))';
            stats(i,iq,ip) = regstats(ytmp,lscal,'linear','beta');
        end
    end
end


function [wc,wcx,scal,max_wbox] = wtmm(x,npt,ig)
% *** Important parameters: results of jmm is based entirely on
% *** timews, ratio, maxscal, dscal
timews=8;
ratio=1/8;
minscal=2;
maxscal=ratio*.5*(npt-1)/timews;
dscal=2^0.05;
nscal=fix((log2(maxscal)-log2(minscal))/log2(dscal));
scal=minscal*dscal.^[0:nscal-1];
max_wbox=fix(timews*maxscal);


[c,c0,dc0]=WCmodulus_gaus(x,npt,scal,max_wbox,timews,ig);
[nr,nc]=size(c);
wc=zeros(nr,nc);
```

```matlab
wcx=zeros(nr,nc);
maxwc=zeros(1,nc);
maxwcx=zeros(1,nc);

id=(max_wbox+1):(npt-max_wbox-1);
id0=id+1;
idp1=id0+1;
idm1=id0-1;
for i=1:nscal
    % find local max; NOT yet the max along max-line!
    idmx=find((((c(i,id0)-c(i,idm1))>0) & ((c(i,idp1)-
c(i,id0))<0))==1)+1+max_wbox;
    nmax=length(idmx);
    wc(i,1:nmax)=c(i,idmx);
    wcx(i,1:nmax)=idmx;
    if i==1
        nmxl(i)=nmax;
        maxwc(1:nmax)=wc(i,1:nmax);
        maxwcx(1:nmax)=wcx(i,1:nmax);
    else
        for k=1:nmax
            dd=abs(wcx(i,k)-maxwcx(1:nmxl(i-1)));
            id=find(dd==min(dd));
            if length(id)>1,id=id(1);end
            m21(k,:)=[k id];
        end
        m22=zeros(nmax,2);
        %differences here
        for k=1:nmax
            dd=abs(maxwcx(m21(k,2))-wcx(i,1:nmax));
            id=find(dd==min(dd));
            if length(id)>1,id=id(1);end
            if id==m21(k,1)
                m22(k,:)=m21(k,:);
            else
                m22(k,:)=[0 0];
            end
        end
        m22(find(sum(m22')==0),:)=[];
        [nr1,nc1]=size(m22);
        nmxl(i)=nr1;
        wcx(i,1:nr1)=wcx(i,m22(:,1));
        wc(i,1:nr1)=wc(i,m22(:,1));
        wc(i,1:nr1)=max(wc(i,1:nr1),maxwc(m22(:,2)));
        wc(i,nr1+1:end)=0;
        wcx(i,nr1+1:end)=0;
        maxwc(1:nr1)=wc(i,1:nr1);
        maxwcx(1:nr1)=wcx(i,1:nr1);
    end
end


function [c,c0,dc0]=WCmodulus_gaus(x,npt,a,max_wbox,timews,ig)

nscal=length(a);
```

```matlab
Nx = npt-2*max_wbox-1;
c0 = zeros(nscal,npt);
dc0 = zeros(nscal,npt);
idbx = max_wbox+1:npt-max_wbox-1;
for i = 1:nscal
    half_wbox=fix(timews*a(i));
    [psiax,dpsiax] = getwlet(a(i),half_wbox,ig);
    for b = idbx
        id = [b-half_wbox:b+half_wbox]+1;
        c0(i,b) = sum(x(id).*psiax(id-b+half_wbox));
        dc0(i,b) = sum(x(id).*dpsiax(id-b+half_wbox));
    end
    c0(i,:)=c0(i,:)./a(i);
    c(i,:)=abs(c0(i,:));
end

% ************** END WCmodulus_gaus *****************

function    [psiax,dpsiax]=getwlet(a,half_wbox,ig)

g1=inline('-exp(-.5.*t.^2).*t','t');
dg1=inline('-t.*exp(-.5.*t.^2).*(t.^2-2)./s','t','s');
g2=inline('exp(-.5.*t.^2).*(t.^2-1)','t');
dg2=inline('exp(-.5.*t.^2).*(t.^4-4.*t.^2+1)./s','t','s');
g3=inline('t.*exp(-.5.*t.^2).*(3-t.^2)','t');
dg3=inline('-t.*exp(-.5.*t.^2).*(t.^4-7.*t.^2+6)./s','t','s');
g4=inline('exp(-.5.*t.^2).*(t.^4-6.*t.^2+3)','t');
dg4=inline('exp(-.5.*t.^2).*(t.^6-11.*t.^4+21.*t.^2-3)./s','t','s');

t=([0:2*half_wbox]-half_wbox)./a;

switch ig
    case 1
        psiax=g1(t);
        dpsiax=dg1(t,a);
    case 2
        psiax=g2(t);
        dpsiax=dg2(t,a);
    case 3
        psiax=g3(t);
        dpsiax=dg3(t,a);
    case 4
        psiax=g4(t);
        dpsiax=dg4(t,a);
    otherwise
        disp('no data');
        return;
end
```

References

1. Benzi, R., Paladin, G., Parisi, G. & Vulpiani, A. On the Multifractal Nature of Fully-Developed Turbulence and Chaotic Systems. *Journal of Physics A-Mathematical and General* **17**, 3521-3531 (1984).

2. Smalley, R. F., Chatelain, J. L., Turcotte, D. L. & Prevot, R. A Fractal Approach to the Clustering of Earthquakes - Applications to the Seismicity of the New Hebrides. *Bulletin of the Seismological Society of America* **77**, 1368-1381 (1987).

3. Hamilton, M. J., Milne, B. T., Walker, R. S., Burger, O. & Brown, J. H. The complex structure of hunter-gatherer social networks. *Proceedings of the Royal Society B-Biological Sciences* **274**, 2195-2202 (2007).

4. Zhou, W. X., Sornette, D., Hill, R. A. & Dunbar, R. I. M. Discrete hierarchical organization of social group sizes. *Proceedings of the Royal Society B-Biological Sciences* **272**, 439-444 (2005).

5. Arneodo, A., Audit, B., Bacry, E., Manneville, S., Muzy, J. F. & Roux, S. G. Thermodynamics of fractal signals based on wavelet analysis: application to fully developed turbulence data and DNA sequences. *Physica A-Statistical Mechanics and its Applications* **254**, 24-45 (1998).

6. Nottale, L. Fractals and the Quantum-Theory of Spacetime. *Int. J. Mod. Phys. A* **4**, 5047-5117 (1989).

7. Hausdorff, J. M., Peng, C. K., Ladin, Z., Wei, J. Y. & Goldberger, A. L. Is Walking a Random-Walk - Evidence for Long-Range Correlations in Stride Interval of Human Gait. *J. Appl. Physiol.* **78**, 349-358 (1995).

8. Mantegna, R. N. & Stanley, H. E. Stock market dynamics and turbulence: Parallel analysis of fluctuation phenomena. *Physica a* **239**, 255-266 (1997).

9. Naoko, S., Mizuno, M., Nishida, Y., Nagaya, R., Harada, T., Tanaka, H., Quistorff, B. & Saltin, B. Influence of mild exercise training on skeletal muscle capillary density and serum lipid levels. *J. Aging Phys. Act.* **8**, 274-274 (2000).

10. Amaral, L. A. N., Ivanov, P. C., Aoyagi, N., Hidaka, I., Tomono, S., Goldberger, A. L., Stanley, H. E. & Yamamoto, Y. Behavioral-independence features of complex heartbeat dynamics. *Phys. Rev. Lett.* **86**, 6026-6029 (2001).

11. Camm, A. J., Malik, M., Bigger, J. T., Breithardt, G., Cerutti, S., Cohen, R. J., Coumel, P., Fallen, E. L., Kennedy, H. L., Kleiger, R. E., Lombardi, F., Malliani, A., Moss, A. J., Rottman, J. N., Schmidt, G., Schwartz, P. J. & Singer, D. H. Heart rate variability. Standards of measurement, physiological interpretation, and clinical use. *Eur. Heart J.* **17**, 354-381 (1996).

12. Huikuri, H. V. & Makikallio, T. H. Heart rate variability in ischemic heart disease. *Autonomic Neuroscience-Basic & Clinical* **90**, 95-101 (2001).

13. Goldberger, A. L., Amaral, L. A. N., Hausdorff, J. M., Ivanov, P. C., Peng, C. K. & Stanley, H. E. Fractal dynamics in physiology: Alterations with disease and aging. *Proc. Natl. Acad. Sci. U. S. A.* **99**, 2466-2472 (2002).

14. Makikallio, T. H., Huikuri, H. V., Makikallio, A., Sourander, L. B., Mitrani, R. D., Castellanos, A. & Myerburg, R. J. Prediction of sudden cardiac death by fractal analysis of heart rate variability in elderly subjects. *J. Am. Coll. Cardiol.* **37**, 1395-1402 (2001).

15. Iyengar, N., Peng, C. K., Morin, R., Goldberger, A. L. & Lipsitz, L. A. Age-related alterations in the fractal scaling of cardiac interbeat interval dynamics. *Am. J. Physiol.* **271**, R1078-84 (1996).

16. Pikkujamsa, S. M., Makikallio, T. H., Sourander, L. B., Raiha, I. J., Puukka, P., Skytta, J., Peng, C. K., Goldberger, A. L. & Huikuri, H. V. Cardiac interbeat interval dynamics from childhood to senescence : comparison of conventional and new measures based on fractals and chaos theory. *Circulation* **100**, 393-399 (1999).

17. Gisiger, T. Scale invariance in biology: coincidence or footprint of a universal mechanism? *Biol. Rev. Camb. Philos. Soc.* **76**, 161-209 (2001).

18. Bacry, E., Muzy, J. F. & Arneodo, A. Singularity Spectrum of Fractal Signals from Wavelet Analysis - Exact Results. *Journal of Statistical Physics* **70**, 635-674 (1993).

19. Hwang, W. & Mallat, S. Characterization of self-similar multifractals with wavelet maxima. *Applied and Computational Harmonic Analysis* **1**, 316-328 (1994).

20. Kumada, M., Terui, N. & Kuwaki, T. Arterial Baroreceptor Reflex - its Central and Peripheral Neural Mechanisms. *Prog. Neurobiol.* **35**, 331-361 (1990).

21. Fortrat, J. O., Yamamoto, Y. & Hughson, R. L. Respiratory influences on non-linear dynamics of heart rate variability in humans. *Biol. Cybern.* **77**, 1-10 (1997).

22. Fortrat, J. O., Sigaudo, D., Hughson, R. L., Maillet, A., Yamamoto, Y. & Gharib, C. Effect of prolonged head-down bed rest on complex cardiovascular dynamics. *Autonomic Neuroscience-Basic & Clinical* **86**, 192-201 (2001).

23. Dampney, R. A. L. Functional-Organization of Central Pathways Regulating the Cardiovascular-System. *Physiol. Rev.* **74**, 323-364 (1994).

24. Berntson, G. G. & Cacioppo, J. T. Heart Rate Variability: A Neuroscientific Perspective for Further Studies. **3**, 282 (1999).

25. Dampney, R. A., Coleman, M. J., Fontes, M. A., Hirooka, Y., Horiuchi, J., Li, Y. W., Polson, J. W., Potts, P. D. & Tagawa, T. Central mechanisms underlying short- and long-term regulation of the cardiovascular system. *Clin. Exp. Pharmacol. Physiol.* **29**, 261-268 (2002).

26. Borresen, J. & Lambert, M. I. Autonomic control of heart rate during and after exercise : measurements and implications for monitoring training status. *Sports Med.* **38**, 633-646 (2008).

27. Brandenberger, G., Ehrhart, J., Piquard, F. & Simon, C. Inverse coupling between ultradian oscillations in delta wave activity and heart rate variability during sleep. *Clinical Neurophysiology* **112**, 992-996 (2001).

28. van den Berg, J., Neely, G., Wiklund, U. & Landstrom, U. Heart rate variability during sedentary work and sleep in normal and sleep-deprived states. *Clin. Physiol. Funct. Imaging* **25**, 51-57 (2005).

29. Inanaga, K. Frontal midline theta rhythm and mental activity. *Psychiatry Clin. Neurosci.* **52**, 555-566 (1998).

30. Bunde, A., Havlin, S., Kantelhardt, J. W., Penzel, T., Peter, J. H. & Voigt, K. Correlated and uncorrelated regions in heart-rate fluctuations during sleep. *Phys. Rev. Lett.* **85**, 3736-3739 (2000).

31. Lin, D. C. & Sharif, A. Wavelet transform modulus maxima based fractal correlation analysis. *European Physical Journal B* **60**, 483-491 (2007).

32. Kollai, M. & Mizsei, G. Respiratory Sinus Arrhythmia is a Limited Measure of Cardiac Parasympathetic Control in Man. *Journal of Physiology-London* **424**, 329-342 (1990).

33. Malliani, A. in *Principles of cardiovascular neural regulation in health and disease* 222 (Kluwer Academic, Boston, Mass., 2000).

34. Zucker, I. H., Wang, W., Brandle, M., Schultz, H. D. & Patel, K. P. Neural regulation of sympathetic nerve activity in heart failure. *Prog. Cardiovasc. Dis.* **37**, 397-414 (1995).

35. Montano, N., Porta, A., Cogliati, C., Costantino, G., Tobaldini, E., Casali, K. R. & Iellamo, F. Heart rate variability explored in the frequency domain: a tool to investigate the link between heart and behavior. *Neurosci. Biobehav. Rev.* **33**, 71-80 (2009).

36. Yamamoto, Y., Nakamura, Y., Sato, H., Yamamoto, M., Kato, K. & Hughson, R. L. On the fractal nature of heart rate variability in humans: effects of vagal blockade. *Am. J. Physiol.* **269**, R830-7 (1995).

37. Ter Horst, G. J. & Postema, F. Forebrain parasympathetic control of heart activity: retrograde transneuronal viral labeling in rats. *Am. J. Physiol.* **273**, H2926-30 (1997).

38. Verberne, A. J. Medullary sympathoexcitatory neurons are inhibited by activation of the medial prefrontal cortex in the rat. *Am. J. Physiol.* **270**, R713-9 (1996).

39. Ahern, G. L., Sollers, J. J., Lane, R. D., Labiner, D. M., Herring, A. M., Weinand, M. E., Hutzler, R. & Thayer, J. F. Heart rate and heart rate variability changes in the intracarotid sodium amobarbital test. *Epilepsia* **42**, 912-921 (2001).

40. Lane, R. D., McRae, K., Reiman, E. M., Chen, K., Ahern, G. L. & Thayer, J. F. Neural correlates of heart rate variability during emotion. *Neuroimage* **44**, 213-222 (2009).

41. Gianaros, P. J., Van Der Veen, F. M. & Jennings, J. R. Regional cerebral blood flow correlates with heart period and high-frequency heart period variability during working-memory tasks: Implications for the cortical and subcortical regulation of cardiac autonomic activity. *Psychophysiology* **41**, 521-530 (2004).

42. Ziegler, G., Dahnke, R., Yeragani, V. K. & Bar, K. J. The relation of ventromedial prefrontal cortex activity and heart rate fluctuations at rest. *Eur. J. Neurosci.* **30**, 2205-2210 (2009).

43. Saha, S. Role of the central nucleus of the amygdala in the control of blood pressure: descending pathways to medullary cardiovascular nuclei. *Clin. Exp. Pharmacol. Physiol.* **32**, 450-456 (2005).

44. Green, A. L., Wang, S., Owen, S. L. & Aziz, T. Z. The periaqueductal grey area and the cardiovascular system. *Acta Neurochir. Suppl.* **97**, 521-528 (2007).

45. Thayer, J. F., Hansen, A. L., Saus-Rose, E. & Johnsen, B. H. Heart rate variability, prefrontal neural function, and cognitive performance: the neurovisceral integration perspective on self-regulation, adaptation, and health. *Ann. Behav. Med.* **37**, 141-153 (2009).

46. Ally, A. Ventrolateral medullary control of cardiovascular activity during muscle contraction. *Neurosci. Biobehav. Rev.* **23**, 65-86 (1998).

47. Lawrence, A. J. & Jarrott, B. Neurochemical modulation of cardiovascular control in the nucleus tractus solitarius. *Prog. Neurobiol.* **48**, 21-53 (1996).

48. Evrengul, H., Tanriverdi, H., Dursunoglu, D., Kaftan, A., Kuru, O., Unlu, U. & Kilic, M. Time and frequency domain analyses of heart rate variability in patients with epilepsy. *Epilepsy Res.* **63**, 131-139 (2005).

49. Tomson, T., Nashef, L. & Ryvlin, P. Sudden unexpected death in epilepsy: current knowledge and future directions. *Lancet Neurology* **7**, 1021-1031 (2008).

50. Sevcencu, C. & Struijk, J. J. Autonomic alterations and cardiac changes in epilepsy. *Epilepsia* **51**, 725-737 (2010).

51. Singh, D., Vinod, K., Saxena, S. C. & Deepak, K. K. Effects of RR segment duration on HRV spectrum estimation. *Physiol. Meas.* **25**, 721-735 (2004).

52. Galluzzi, S., Nicosia, F., Geroldi, C., Alicandri, A., Bonetti, M., Romanelli, G., Zulli, R. & Frisoni, G. B. Cardiac Autonomic Dysfunction Is Associated With White Matter Lesions in Patients With Mild Cognitive Impairment. *Journals of Gerontology Series A-Biological Sciences and Medical Sciences* **64**, 1312-1315 (2009).

53. Oppenheimer, S. M., Kedem, G. & Martin, W. M. Left-insular cortex lesions perturb cardiac autonomic tone in humans. *Clin. Auton. Res.* **6**, 131-140 (1996).

54. Cooper, R. in *EEG technology* (eds Shaw, J. C. & Osselton, J. W.) (Butterworths, London, 1974).

55. Akselrod, S., Gordon, D., Ubel, F. A., Shannon, D. C., Berger, A. C. & Cohen, R. J. Power spectrum analysis of heart rate fluctuation: a quantitative probe of beat-to-beat cardiovascular control. *Science* **213**, 220-222 (1981).

56. Troncoso, E., Rodriguez, M. & Feria, M. Light-Induced Arousal Affects Simultaneously Eeg and Heart-Rate-Variability in the Rat. *Neurosci. Lett.* **188**, 167-170 (1995).

57. Meneveau, C., Sreenivasan, K. R., Kailasnath, P. & Fan, M. S. Joint multifractal measures: theory and applications to turbulence. *Physical Review A (Statistical Physics, Plasmas, Fluids, and Related Interdisciplinary Topics)* **41**, 894-913 (1990).

58. Riedi, R. H. & Scheuring, I. Conditional and relative multifractal spectra. *Fractals-an Interdisciplinary Journal on the Complex Geometry of Nature* **5**, 153-168 (1997).

59. Lin, D. C. Factorization of joint multifractality. *Physica A-Statistical Mechanics and its Applications* **387**, 3461-3470 (2008).

60. Sharif, A. H. Ryerson University. *Multifractal correlation using wavelet transform modulus maxima* 48, (2006).

61. Olufsen, M. S., Alston, A. V., Tran, H. T., Ottesen, J. T. & Novak, V. Modeling heart rate regulation - Part I: Sit-to-stand versus head-up tilt. *Cardiovascular Engineering* **8**, 73-87 (2008).

62. Cooke, W. H., Hoag, J. B., Crossman, A. A., Kuusela, T. A., Tahvanainen, K. U. O. & Eckberg, D. L. Human responses to upright tilt: a window on central autonomic integration. *Journal of Physiology-London* **517**, 617-628 (1999).

63. Butler, G. C., Yamamoto, Y. & Hughson, R. L. Fractal Nature of Short-Term Systolic Bp and Hr Variability during Lower-Body Negative-Pressure. *Am. J. Physiol.* **267**, R26-R33 (1994).

64. Ishibashi, K., Ueda, S. & Yasukouchi, A. Effects of mental task on heart rate variability during graded head-up tilt. *Appl. Human Sci.* **18**, 225-231 (1999).

65. Ammirati, F., Colivicchi, F., Di Battista, G., Garelli, F. F. & Santini, M. Electroencephalographic correlates of vasovagal syncope induced by head-up tilt testing. *Stroke* **29**, 2347-2351 (1998).

66. Mercader, M. A., Varghese, P. J., Potolicchio, S. J., Venkatraman, G. K. & Lee, S. W. New insights into the mechanism of neurally mediated syncope. *Heart* **88**, 217-221 (2002).

67. Grieve, P. G., Myers, M. M., Stark, R. I., Housman, S. & Fifer, W. P. Topographic localization of electrocortical activation in newborn and two- to four-month-old infants in response to head-up tilting. *Acta Paediatr.* **94**, 1756-1763 (2005).

68. Vybiral, T., Bryg, R. J., Maddens, M. E. & Boden, W. E. Effect of passive tilt on sympathetic and parasympathetic components of heart rate variability in normal subjects. *Am. J. Cardiol.* **63**, 1117-1120 (1989).

69. Phongsuphap, S., Pongsupap, Y., Chandanamattha, P. & Lursinsap, C. Changes in heart rate variability during concentration meditation. *Int. J. Cardiol.* **130**, 481-484 (2008).

70. Tulppo, M. P., Hughson, R. L., Makikallio, T. H., Airaksinen, K. E., Seppanen, T. & Huikuri, H. V. Effects of exercise and passive head-up tilt on fractal and complexity properties of heart rate dynamics. *Am. J. Physiol. Heart Circ. Physiol.* **280**, H1081-7 (2001).

71. Niedermeyer, E. & Lopes da Silva, F. H. Electroencephalography. , 1309 (2005).

72. Nunez, P. L. & Srinivasan, R. in *Electric fields of the brain : the neurophysics of EEG* 611 (Oxford University Press, New York, 2006).

73. Klem, G. H., Luders, H. O., Jasper, H. H. & Elger, C. The ten-twenty electrode system of the International Federation. The International Federation of Clinical Neurophysiology. *Electroencephalogr Clin Neurophysiol Suppl.* **52**, 3-6 (1999).

74. Levick, J. R. in *An introduction to cardiovascular physiology* 433 (Arnold; Oxford University Press, London; New York, 2000).

75. Ferree, T. C., Luu, P., Russell, G. S. & Tucker, D. M. Scalp electrode impedance, infection risk, and EEG data quality. *Clin. Neurophysiol.* **112**, 536-544 (2001).

76. Tatum, W. O. & ebrary, I. Handbook of EEG interpretation. , 276 (2008).

77. Croft, R. J. & Barry, R. J. Removal of ocular artifact from the EEG: a review. *Neurophysiologie Clinique-Clinical Neurophysiology* **30**, 5-19 (2000).

78. Fatourechi, M., Bashashati, A., Ward, R. K. & Birch, G. E. EMG and EOG artifacts in brain computer interface systems: A survey. *Clinical Neurophysiology* **118**, 480-494 (2007).

79. Zhang, X. P. & Desai, M. D. Adaptive denoising based on SURE risk. *IEEE Signal Process. Lett.* **5**, 265-267 (1998).

80. Krishnaveni, V., Jayaraman, S., Anitha, L. & Ramadoss, K. Removal of ocular artifacts from EEG using adaptive thresholding of wavelet coefficients. *Journal of Neural Engineering* **3**, 338-346 (2006).

81. Aoyagi, N., Ohashi, K. & Yamamoto, Y. Frequency characteristics of long-term heart rate variability during constant-routine protocol. *American Journal of Physiology-Regulatory Integrative and Comparative Physiology* **285**, R171-R176 (2003).

82. Malliani, A., Pagani, M., Lombardi, F. & Cerutti, S. Cardiovascular Neural Regulation Explored in the Frequency-Domain. *Circulation* **84**, 482-492 (1991).

83. Lomb, N. R. Least-Squares Frequency-Analysis of Unequally Spaced Data. *Astrophysics and Space Science* **39**, 447-462 (1976).

84. Laguna, P., Moody, G. B. & Mark, R. G. Power spectral density of unevenly sampled data by least-square analysis: performance and application to heart rate signals. *Biomedical Engineering, IEEE Transactions on* **45**, 698-715 (1998).

85. Watson, C. G., Jacobs, L. & Herder, J. Correlates of alpha, beta and theta wave production. *J. Clin. Psychol.* **35**, 364-369 (1979).

86. Poupard, L., Sartene, R. & Wallet, J. C. Scaling behavior in beta-wave amplitude modulation and its relationship to alertness. *Biol. Cybern.* **85**, 19-26 (2001).

87. Caldwell, J. A., Prazinko, B. & Caldwell, J. L. Body posture affects electroencephalographic activity and psychomotor vigilance task performance in sleep-deprived subjects. *Clin. Neurophysiol.* **114**, 23-31 (2003).

88. The Mathworks Inc. Matlab. **7.8.0** (2009).

89. Daubechies, I. in *Ten lectures on wavelets* 357 (Society for Industrial and Applied Mathematics, Philadelphia, Pa., 1992).

90. Tien, C. L. & Lienhard, J. H. in *Statistical thermodynamics* 397 (Hemisphere Pub. Co., Washington, 1979).

91. Hurst, H. E., Black, R. P. & Simaika, Y. M. in *Long-term storage, an experimental study* 145 (Constable, London, 1965).

92. Mandelbrot, B. B. in *The fractal geometry of nature* 468 (W.H. Freeman, New York, 1983).

93. Peng, C. K., Buldyrev, S. V., Havlin, S., Simons, M., Stanley, H. E. & Goldberger, A. L. Mosaic Organization of Dna Nucleotides. *Physical Review E* **49**, 1685-1689 (1994).

94. Vehel, J. L. & Vojak, R. Multifractal analysis of Choquet capacities. *Advances in Applied Mathematics* **20**, 1-43 (1998).

95. Cole, J. Relative multifractal analysis. *Chaos Solitons & Fractals* **11**, 2233-2250 (2000).

96. Kant, K. On aggregate traffic generation with multifractal properties. *Global Telecommunications Conference, 1999. GLOBECOM '99* **2; 2**, 1179-1183 vol.2 (1999).

97. Julien, C. The enigma of Mayer waves: Facts and models. *Cardiovasc. Res.* **70**, 12-21 (2006).

98. Castiglioni, P., Di Rienzo, M., Veicsteinas, A., Parati, G. & Merati, G. Mechanisms of blood pressure and heart rate variability: an insight from low-level paraplegia. *Am. J. Physiol. Regul. Integr. Comp. Physiol.* **292**, R1502-9 (2007).

99. Elstad, M., Toska, K., Chon, K. H., Raeder, E. A. & Cohen, R. J. Respiratory sinus arrhythmia: opposite effects on systolic and mean arterial pressure in supine humans. *J. Physiol.* **536**, 251-259 (2001).

100. Adrian, E. D. & Matthews, B. H. The interpretation of potential waves in the cortex. *J. Physiol.* **81**, 440-471 (1934).

101. Moosmann, M., Ritter, P., Krastel, I., Brink, A., Thees, S., Blankenburg, F., Taskin, B., Obrig, H. & Villringer, A. Correlates of alpha rhythm in functional magnetic resonance imaging and near infrared spectroscopy. *Neuroimage* **20**, 145-158 (2003).

102. Inouye, T., Shinosaki, K., Yagasaki, A. & Shimizu, A. Spatial distribution of generators of alpha activity. *Electroencephalogr. Clin. Neurophysiol.* **63**, 353-360 (1986).

103. Basar, E., Schurmann, M., Basar-Eroglu, C. & Karakas, S. Alpha oscillations in brain functioning: an integrative theory. *Int. J. Psychophysiol.* **26**, 5-29 (1997).

104. Halgren, E., Boujon, C., Clarke, J., Wang, C. & Chauvel, P. Rapid distributed fronto-parieto-occipital processing stages during working memory in humans. *Cereb. Cortex* **12**, 710-728 (2002).

105. Lin, D. C., Sharif, A. & Kwan, H. C. Scaling and organization of electroencephalographic background activity and alpha rhythm in healthy young adults. *Biol. Cybern.* **95**, 401-411 (2006).

106. Baker, S. N. Oscillatory interactions between sensorimotor cortex and the periphery. *Curr. Opin. Neurobiol.* **17**, 649-655 (2007).

107. Lalo, E., Gilbertson, T., Doyle, L., Di Lazzaro, V., Cioni, B. & Brown, P. Phasic increases in cortical beta activity are associated with alterations in sensory processing in the human. *Exp. Brain Res.* **177**, 137-145 (2007).

108. Crone, N. E., Miglioretti, D. L., Gordon, B., Sieracki, J. M., Wilson, M. T., Uematsu, S. & Lesser, R. P. Functional mapping of human sensorimotor cortex with electrocorticographic spectral analysis - I. Alpha and beta event-related desynchronization. *Brain* **121**, 2271-2299 (1998).

109. Kirk, I. J. Frequency modulation of hippocampal theta by the supramammillary nucleus, and other hypothalamo-hippocampal interactions: mechanisms and functional implications. *Neurosci. Biobehav. Rev.* **22**, 291-302 (1998).

110. Aftanas, L. I., Savotina, L. N., Makhnev, V. P. & Reva, N. V. Analysis of evoked EEG synchronization and desynchronization during perception of emotiogenic stimuli: association with autonomic activation processes. *Neurosci. Behav. Physiol.* **35**, 951-957 (2005).

111. Butler, G. C., Yamamoto, Y., Xing, H. C., Northey, D. R. & Hughson, R. L. Heart-Rate-Variability and Fractal Dimension during Orthostatic Challenges. *J. Appl. Physiol.* **75**, 2602-2612 (1993).

112. Kubo, Y., Murakami, S., Matsuoka, O., Hotta, N., Oinuma, S., Shinagawa, M., Omori, K., Nunoda, S., Otsuka, K., Ohkawa, S., Cornelissen, G. & Halberg, F. Toward chronocardiologic and chronomic insights: dynamics of heart rate associated with head-up tilting. *Biomed. Pharmacother.* **57 Suppl 1**, 110s-115s (2003).

113. Mourot, L., Bouhaddi, M., Gandelin, E., Cappelle, S., Nguyen, N. U., Wolf, J. P., Rouillon, J. D., Hughson, R. & Regnard, J. Conditions of autonomic reciprocal interplay versus autonomic co-activation: effects on non-linear heart rate dynamics. *Auton. Neurosci.* **137**, 27-36 (2007).

114. Ivanov, P. C., Amaral, L. A. N., Goldberger, A. L., Havlin, S., Rosenblum, M. G., Struzik, Z. R. & Stanley, H. E. Multifractality in human heartbeat dynamics. *Nature* **399**, 461-465 (1999).

115. Watters, P. A. Time-invariant long-range correlations in electroencephalogram dynamics. *Int. J. Syst. Sci.* **31**, 819-825 (2000).

116. Hwa, R. C. & Ferree, T. C. Scaling properties of fluctuations in the human electroencephalogram. *Physical Review E* **66** (2002).

117. Stam, C. J. & de Bruin, E. A. Scale-free dynamics of global functional connectivity in the human brain. *Hum. Brain Mapp.* **22**, 97-109 (2004).

118. Linkenkaer-Hansen, K., Nikouline, V. V., Palva, J. M. & Ilmoniemi, R. J. Long-range temporal correlations and scaling behavior in human brain oscillations. *Journal of Neuroscience* **21**, 1370-1377 (2001).

119. Bhattacharya, J., Kanjilal, P. P. & Nizamie, S. H. Decomposition of posterior alpha rhythm. *Ieee Transactions on Biomedical Engineering* **47**, 738-747 (2000).

120. Freeman, W. J. Origin, structure, and role of background EEG activity. Part 2. Analytic phase. *Clinical Neurophysiology* **115**, 2089-2107 (2004).

121. Serrano, E. & Figliola, A. Wavelet Leaders: A new method to estimate the multifractal singularity spectra. *Physica A-Statistical Mechanics and its Applications* **388**, 2793-2805 (2009).

122. Polonnikov, R. I., Wasserman, E. L. & Kartashev, N. K. Regular developmental changes in EEG multifractal characteristics. *Int. J. Neurosci.* **113**, 1615-1639 (2003).

123. Weiss, B., Clemens, Z., Bodizs, R., Vago, Z. & Halasz, P. Spatio-temporal analysis of monofractal and multifractal properties of the human sleep EEG. *J. Neurosci. Methods* **185**, 116-124 (2009).

124. Schreiber, T. & Schmitz, A. Surrogate time series. *Physica D-Nonlinear Phenomena* **142**, 346-382 (2000).

125. Theiler, J., Eubank, S., Longtin, A., Galdrikian, B. & Farmer, J. D. Testing for Nonlinearity in Time-Series - the Method of Surrogate Data. *Physica D* **58**, 77-94 (1992).

126. Schreiber, T. & Schmitz, A. Improved surrogate data for nonlinearity tests. *Phys. Rev. Lett.* **77**, 635-638 (1996).

127. Lipsitz, L. A., Mietus, J., Moody, G. B. & Goldberger, A. L. Spectral characteristics of heart rate variability before and during postural tilt. Relations to aging and risk of syncope. *Circulation* **81**, 1803-1810 (1990).

128. Zhou, W. X. The components of empirical multifractality in financial returns. *Epl* **88** (2009).

129. Francis, D. P., Willson, K., Georgiadou, P., Wensel, R., Davies, L. C., Coats, A. & Piepoli, M. Physiological basis of fractal complexity properties of heart rate variability in man. *J. Physiol.* **542**, 619-629 (2002).

130. Yamamoto, Y., LaManca, J. J. & Natelson, B. H. A measure of heart rate variability is sensitive to orthostatic challenge in women with chronic fatigue syndrome. *Exp. Biol. Med. (Maywood)* **228**, 167-174 (2003).

131. Butler, G. C., Yamamoto, Y., Xing, H. C., Northey, D. R. & Hughson, R. L. Heart rate variability and fractal dimension during orthostatic challenges. *J. Appl. Physiol.* **75**, 2602-2612 (1993).

132. Pincus, S. M. Approximate entropy as a measure of system complexity. *Proc. Natl. Acad. Sci. U. S. A.* **88**, 2297-2301 (1991).

133. Yu, X., Zhang, J., Xie, D., Wang, J. & Zhang, C. Relationship between scalp potential and autonomic nervous activity during a mental arithmetic task. *Auton. Neurosci.* **146**, 81-86 (2009).

134. Cole, R. J. Postural baroreflex stimuli may affect EEG arousal and sleep in humans. *J. Appl. Physiol.* **67**, 2369-2375 (1989).

135. Yamamoto, K., Miyachi, M., Saitoh, T., Yoshioka, A. & Onodera, S. Effects of endurance training on resting and post-exercise cardiac autonomic control. *Med. Sci. Sports Exerc.* **33**, 1496-1502 (2001).

136. Sacknoff, D. M., Gleim, G. W., Stachenfeld, N. & Coplan, N. L. Effect of athletic training on heart rate variability. *Am. Heart J.* **127**, 1275-1278 (1994).

137. Karavirta, L., Hakkinen, A., Sillanpaa, E., Garcia-Lopez, D., Kauhanen, A., Haapasaari, A., Alen, M., Pakarinen, A., Kraemer, W. J., Izquierdo, M., Gorostiaga, E. & Hakkinen, K. Effects of combined endurance and strength training on muscle strength, power and hypertrophy in 40-67-year-old men. *Scand. J. Med. Sci. Sports* (2009).

138. Kubota, Y., Sato, W., Toichi, M., Murai, T., Okada, T., Hayashi, A. & Sengoku, A. Frontal midline theta rhythm is correlated with cardiac autonomic activities during the performance of an attention demanding meditation procedure. *Brain Res. Cogn. Brain Res.* **11**, 281-287 (2001).

139. Tang, Y. Y., Ma, Y., Fan, Y., Feng, H., Wang, J., Feng, S., Lu, Q., Hu, B., Lin, Y., Li, J., Zhang, Y., Wang, Y., Zhou, L. & Fan, M. Central and autonomic nervous system interaction is altered by short-term meditation. *Proc. Natl. Acad. Sci. U. S. A.* **106**, 8865-8870 (2009).

140. Ryan, S. M., Goldberger, A. L., Pincus, S. M., Mietus, J. & Lipsitz, L. A. Gender- and age-related differences in heart rate dynamics: are women more complex than men? *J. Am. Coll. Cardiol.* **24**, 1700-1707 (1994).

141. Huikuri, H. V., Pikkujamsa, S. M., Airaksinen, K. E., Ikaheimo, M. J., Rantala, A. O., Kauma, H., Lilja, M. & Kesaniemi, Y. A. Sex-related differences in autonomic modulation of heart rate in middle-aged subjects. *Circulation* **94**, 122-125 (1996).

142. Hirsch, J. A. & Bishop, B. Respiratory sinus arrhythmia in humans: how breathing pattern modulates heart rate. *Am. J. Physiol.* **241**, H620-9 (1981).

143. Perakakis, P., Taylor, M., Martinez-Nieto, E., Revithi, I. & Vila, J. Breathing frequency bias in fractal analysis of heart rate variability. *Biol. Psychol.* **82**, 82-88 (2009).

144. Bartsch, R., Kantelhardt, J. W., Penzel, T. & Havlin, S. Experimental evidence for phase synchronization transitions in the human cardiorespiratory system. *Phys. Rev. Lett.* **98**, 054102 (2007).

145. Tan, C. O., Cohen, M. A., Eckberg, D. L. & Taylor, J. A. Fractal properties of human heart period variability: physiological and methodological implications. *J. Physiol.* **587**, 3929-3941 (2009).

146. Struzik, Z. R., Hayano, J., Sakata, S., Kwak, S. & Yamamoto, Y. 1/f Scaling in Heart Rate Requires Antagonistic Autonomic Control. *Phys. Rev. E. Stat. Nonlin Soft Matter Phys.* **70**, 050901 (2004).

147. Kotani, K., Struzik, Z. R., Takamasu, K., Stanley, H. E. & Yamamoto, Y. Model for complex heart rate dynamics in health and diseases. *Phys. Rev. E. Stat. Nonlin Soft Matter Phys.* **72**, 041904 (2005).